Simulation Study of Energetic Particle Driven Alfvén Eigenmodes and Geodesic Acoustic Modes in Toroidal Plasmas

WANG, Hao

DOCTOR OF PHILOSOPHY

Department of Fusion Science

School of Physical Sciences

The Graduate University for Advanced Studies

2012

Abstract

Linear properties and nonlinear evolution of energetic particle driven Alfvén eigenmodes and geodesic acoustic modes (GAM) in toroidal plasmas are investigated using a hybrid simulation code for magnetohydrodynamics (MHD) and energetic particles.

The interaction between energetic particles and Alfvén eigenmodes in reversed shear tokamak plasmas are investigated for different minimum safety-factor values. When the energetic particle distribution is isotropic in velocity space, it is demonstrated that the transition from low-frequency reversed shear Alfvén eigenmode (RSAE mode) to toroidal Alfvén eigenmode (TAE mode) takes place as the minimum safety-factor value decreases. The frequency rises up from a level above the GAM frequency to the TAE frequency. It is found that the energetic particles both co- and counter-going to the plasma current are transported by the TAE mode, whereas the co-going particles are primarily transported by the low-frequency RSAE mode. When only the co-passing particles are retained, the low-frequency RSAE modes are primarily destabilized. On the other hand, the high-frequency RSAE modes are destabilized when only the counter-passing particles are retained.

The linear properties and the nonlinear evolution of energetic particle driven GAM (EGAM) are explored for the Large Helical Device (LHD) plasmas. For the linear properties, it is found that the EGAM is a global mode

because the fluctuation frequency is spatially constant, whereas the conventional local GAM frequency constitutes a continuous spectrum that varies depending on the plasma temperature and the safety-factor. The frequency of the EGAM intersects with the GAM continuous spectrum. The EGAM frequency is lower for the higher energetic particle pressure. The poloidal mode numbers of poloidal velocity fluctuation, plasma density fluctuation, and magnetic fluctuation are $m = 0$, 1, and 2, respectively. Good agreement is found between the LHD experiment and the simulation result in the EGAM frequency and the mode numbers. The EGAM spatial profile depends on the energetic particle spatial distribution and the equilibrium magnetic shear. The wider energetic particle spatial profile broadens the EGAM spatial profile. The EGAM spatial profile is wider for the reversed magnetic shear than for the normal shear.

The nonlinear evolution of EGAM is studied using the hybrid simulation code. It is demonstrated that the nonlinear frequency chirping of EGAM takes place in the simulation. The frequency chirping of EGAM has been observed in LHD and tokamaks. In order to clarify the physics mechanism of the frequency chirping, the energetic particle distribution function is analyzed in 2-dimensional velocity space of energy and pitch angle variable. It is found that two pairs of hole and clump are created, one at the destabilizing region and the other at the stabilizing region. The transit frequencies of the holes and clumps are compared with the EGAM frequency. The transit frequencies of the holes and clumps are in good agreement with the two branches of the EGAM frequency, one chirping up and the other chirping down. This indicates that the holes and clumps are kept resonant with the EGAM and the frequency chirping can be attributed to the hole-clump pair creation. The hole-clump pair creation and the associated frequency chirping are known to take place when the system is close to the instability threshold

for the inverse Landau damping. This is the first numerical demonstration of a) hole-clump pair creation and frequency chirping for EGAM, b) two pairs creation at the destabilizing and the stabilizing regions, and c) hole-clump pairs in 2-dimensional velocity space.

Acknowledgements

I would like to thank Professor Yasushi TODO for his careful guidance and warm encouragement during my graduate studies. He takes long time to improve my studies, even if he is very busy with other works. At the beginning of my Ph.D. studies, I knew only a little bit about energetic particle simulation. However, now I am able to defend my dissertation successfully and publish my research results in journals. In order to achieve that, Prof. TODO help me so much that half or more credits should go to him. It is the best decision I made in these 3 years to choose him as my supervisor.

I wish to thank Prof. Naoki MIZUGUCHI, Prof. Charlson C. KIM (Washinton Univ.), Prof. Hideo SUGAMA and Prof. Takeshi IDO (NIFS) for their fruitful discussions. They help me to get better understanding of the results in simulation and experiment.

I would like to thank Prof. Tomohiko WATANABE, Prof. Mitsutaka ISOBE, Prof. Sadayoshi MURAKAMI (Kyoto Univ.) and Prof. Koji SHINOHARA (JAEA). This dissertation is improved with their help. I would also like to thank the referees of the *Journal of the Physical Society of Japan*, the *Physical Review Letters*, and the *Physics of Plasmas*. They gave me so many suggestions and encouragements although I don't know their names.

I would also like to acknowledge Prof. Kazuo TOI, Prof. Masaki OSAKABE (NIFS), Dr. Wei CHEN (SWIP), Dr. Kunihiro OGAWA (JSPS) and

Contents

Chapter 1

Introduction

1.1 Background

The process of human being's living is a series of actions to obtain energy. Today we are facing energy crisis[1]. The world annual energy consumption is about 6×10^{20} joules. If all the energy is supplied by oil, then the oil can be used for only 30 years. Natural gas is the same. Coal is better because it can be used for 500 years, but if we really consume it for several hundreds years, the global warming will be as dangerous as energy crisis. Nuclear power plant doesn't make CO_2 emission, and it can be used for long time. Uranium 235 for fission reactors can be used for only 20 years, but the uranium 238 and thorium 232 for breeder reactors can support 20 thousands years. However, the safety is a trouble. The public fear this kind of plant after Fukushima disaster[2].

Nuclear fusion can resolve the energy problem. Energy can be obtained from D-T (Deuterium-Tritium) reaction:[1, 3]

$$D^2 + T^3 \longrightarrow He^4 + n^1 + 17.6 MeV. \tag{1.1}$$
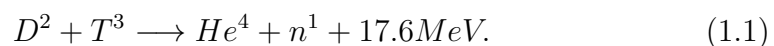
The deuterium can be obtained from the ocean almost infinitely. The tritium

can be produced from lithium (Li):

$$Li^6 + n \longrightarrow T + He^4 + 4.8MeV, \tag{1.2}$$

$$Li^7 + n \longrightarrow T + He^4 + n - 2.5MeV, \tag{1.3}$$
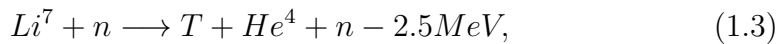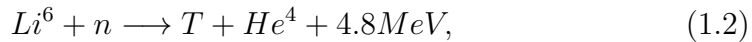
and the resource of Li in our planet can be used for 1×10^7 years, almost forever. In addition, fusion reaction is clean and safe.[1]

Generally speaking, the self-sustaining fusion can be realized in 3 ways: gravity confinement fusion which happens in stars, inertial confinement fusion (ICF), and magnetic confinement fusion (MCF). In laboratories, scientists focus on ICF and MCF. It seems that the MCF is accepted better because there is an international collaboration to build an MCF device, ITER[4]. There are also many MCF devices smaller than ITER, e.g. Large Helical Device (LHD) and tokamaks[1, 4]. In order to realize MCF, high temperature and high density plasma should be confined in magnetic field stably and continually. It is not easy because there are so many instabilities before and after ignition. If these instabilities are excited, the confinement will be challenged even be failed. Some of the instabilities driven by energetic particles draw attention. The toroidal Alfvén eigenmode (TAE), reversed shear Alfvén eigenmode (R-SAE) and energetic particle driven geodesic acoustic mode (EGAM) are 3 kinds of energetic particle driven instabilities investigated in the present thesis.

1.2   Motivation

The energetic particle driven instabilities are important for fusion research because they cause enhanced fast-ion transport leading to deterioration of plasma heating performance. High temperature plasma is essential for self-sustained fusion reaction. The plasma in fusion reactor is mainly heated by

energetic particles which include α particles. The enhanced transport makes the heating worse. In addition, such kind of transport is harmful to the first wall.

The present thesis is mainly focused on TAE, RSAE and EGAM. TAE and RSAE are two kinds of stable magnetohydrodynamics (MHD) modes. They can be destabilized by energetic particles and enhance energetic particles transport as shown in Fig. 1.1[5]. The neutron rate and fast ion D_α (FIDA) densities are lower than the classical predictions. This indicates that the fast ions are lost. In addition, from $t = 0.3s$ to $t = 0.7s$, the neutron rate and FIDA densities are the lowest, and at the same time, the mode amplitudes of TAE and RSAE are the strongest. This implies that the particle loss is caused by TAE and RSAE. Therefore, it is significant to investigate these 2 kinds of Alfvén eigenmodes. The importance of EGAM is similar. Geodesic acoustic mode (GAM) is a kind of electrostatic mode with $n = 0$, and it is a finite frequency oscillatory zonal flow[6, 7, 8, 9]. It can be driven by plasma micro-turbulence, TAE mode, and energetic particles[6, 7, 8, 9, 10, 11, 12, 13, 14, 15, 16]. EGAM can enhance energetic particles transport as shown in Fig. 1.2[12]. In figure (b), the red curve represents the neutron emission and the black one means the mode amplitude of EGAM. The red curve drops 4 times at $t = 316ms, 322ms, 328ms$ and $335ms$, and the 4 drops occur at the same times as 4 pulses of EGAM. The neutron emission is due to the D-D nuclear reaction, and is thus proportional to the fast ion population. This implies that the energetic particles are lost and the loss is caused by EGAM. So it is valuable to study this mode.

The motivation of the present work is to research RSAE, TAE and EGAM by means of simulation. In the case of Alfvén eigenmodes, although a large number of studies have been made, little attention has been paid to the interaction between energetic particles and modes. An important question
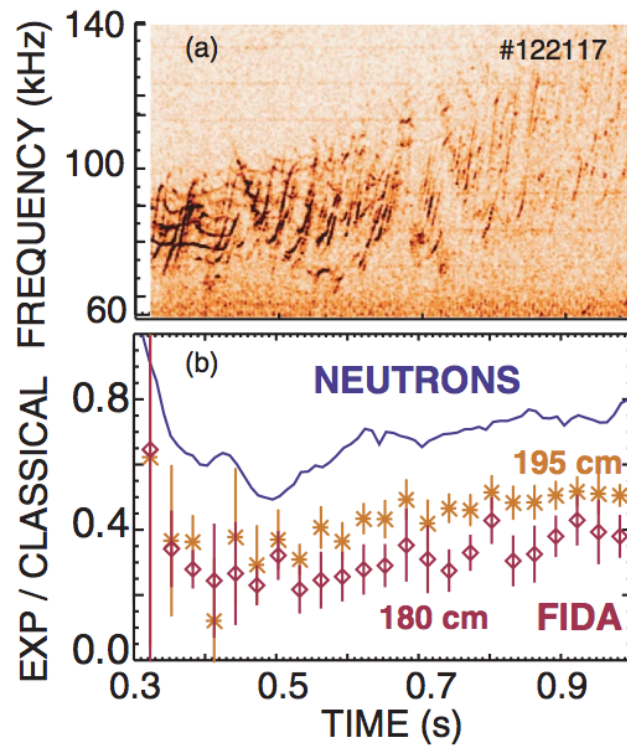
Figure 1.1: The experiment results of TAE and RSAE in the DIII-D toka-mak. (a) TAE and RSAE frequency power spectrum. (b) Neutron rate and FIDA densities. The signals are normalized by the classical TRANSP code prediction and beam-ion density predictions, respectively.[5]
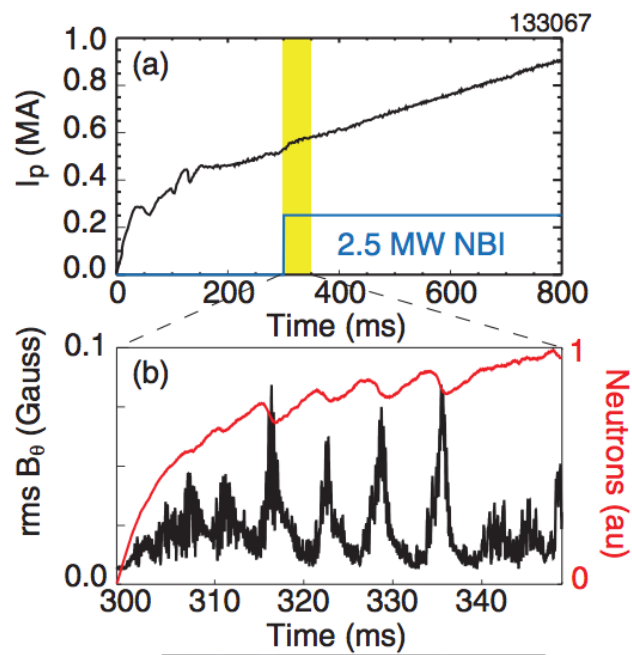
Figure 1.2: Evolution of (a) plasma current I_p and $75keV$ deuterium neutral beam power, (b) edge poloidal magnetic field fluctuations $\tilde{B}_\theta$ and neutron emission n_s in the DIII-D tokamak.[12]

for fusion burning plasmas is whether the energetic-particle transport changes or not when the transition between RSAE and TAE take place. In order to answer this question, it is necessary to compare the RSAE and TAE, and focus on the difference in energetic particle transport. It is the first attempt to investigate the transport differences between RSAE and TAE. For the EGAM case, experimental and theoretical researches are carried out only several years[11, 12, 13, 16, 14, 15]. The mechanism of mode excitation is clarified in different way[11, 13, 14], but there are still many other interesting topics need to be investigated. Many linear properties of EGAM have not been revealed, and the nonlinear frequency chirping of energetic particle driven EGAM need to be explained. In the present thesis, we planned to answer the question what is the properties of EGAM. In addition, to answer what is the mechanism of frequency chirping and how the energetic particle distribution is modified by EGAM. It is the first attempt to reveal EGAM frequency chirping mechanism, and many interesting results are obtained as described in chapter 4.

1.3 Framework of this thesis

The framework of this thesis is shown in Fig. 1.3.

All the results in the present thesis are obtained by means of simulation, so a whole chapter (chapter 2) is devoted to describe the simulation code, MEGA[17, 18]. The basic physical equations that include ideal MHD equations and drift kinetic equations are described, and the coupling between the energetic particles and background plasmas is illustrated. In addition, the computational method, e.g. δf method and the Runge-Kutta method are also described because they are applied in the code. The simulation model is mentioned. The detailed models for Alfvén eigenmode and EGAM are
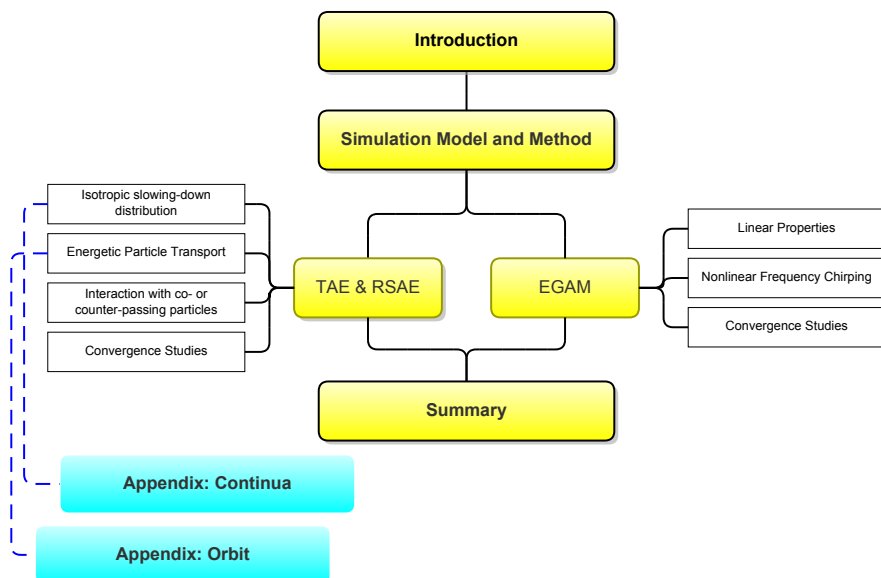
Figure 1.3: The framework of this thesis.

different, and these differences will be shown in chapter 3 and chapter 4, respectively.

The results of Alfvén eigenmode are presented in chapter 3. A brief introduction to the current research of TAE and RSAE appears in the first section. In Sec. 3.2, the simulation model and computational method for Alfvén eigenmode are described. In Sec. 3.3, the simulation results of RSAE modes and TAE modes are shown, and the differences in the energetic particle transport between the two types of eigenmodes are discussed. The results include 4 parts: the results simulated under the isotropic slowing-down distribution, the results of the energetic particle transport, the interaction with co- or counter-passing particles, and the examination of numerical convergence in number of computational particles and time step width. Sec. 3.4 is devoted to summary.

The results of EGAM are presented in chapter 4. This chapter begins with an introduction to the current EGAM studies. In Sec. 4.2, the simulation model and methods for EGAM are presented. Different with the Alfvén eigenmode case, it is necessary to consider distribution function in the pitch angle Λ space for EGAM case. In addition, q profile is also changed to simulate the LHD plasma. In Sec. 4.3.1, the EGAM linear properties that include the frequency, growth rate, mode number and mode spatial width are examined. Different simulation conditions are applied for investigation. In addition, the nonlinear frequency chirping is reproduced in the simulation result. The energetic particle distribution function is investigated in velocity space. Hole-clump pairs are created and their transit frequencies are in good agreement with the EGAM frequency. Numerical convergence in number of computational particles, grid size and time step width is also examined. Section 4.4 is devoted to summary the simulation results of EGAM.

The present thesis is summarized in chapter 5. Some unsolved problems

are also described, and the preliminary proposal for solving these problems are discussed. In appendix A, the continua of TAE and RSAE are compared, and the influence of toroidicity and reversed shear on these modes is clarified. Appendix B is devoted to illustrate how the particle transport takes place near the edge due to Alfvén eigenmodes localized close to the plasma center.

Unless otherwise specified, SI units are employed.

Chapter 2

Simulation Model and Computational Methods

Computer simulation is a third methodology of physics. Three methodologies, theory, experiment, and computer simulation play important roles in different aspect. With the help of theory, scientists are able to understand the nature of various behaviors of plasma and to predict the undiscovered phenomena. Experiment makes contributions in another way. The theory must be tested by experiment, and the new hot research topics often begin from the new experimental observations. But some of the problems can be hardly investigated thoroughly neither by theory nor by experiment, for example, the nonlinear evolution of many modes, and the evolution of distribution function in phase space. These problems are normally investigated by computer simulation. The cooperation between the theorists, experimenters and the simulation researchers yields profound and original insights of plasma physics.
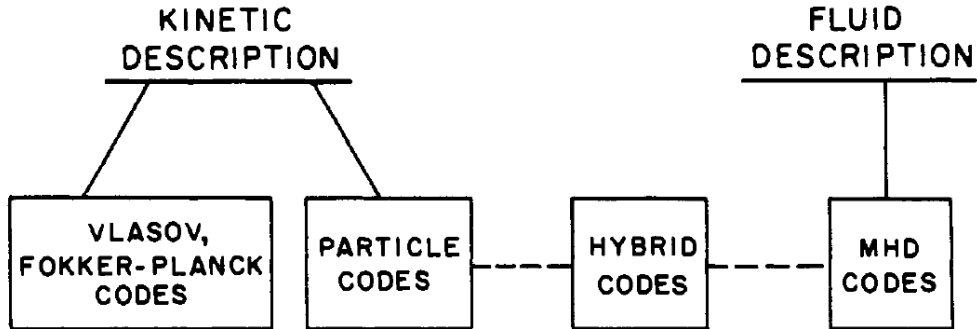
Figure 2.1: Classification of computer simulation models of plasmas.[19]

2.1   Brief introduction of MEGA code

Computer simulation of plasmas comprises two general areas based on kinetic and fluid descriptions, as shown in Fig. 2.1[19]. While fluid simulation proceeds by solving numerically the magnetohydrodynamics (MHD) equations of plasma, kinetic simulation considers more detailed models of the plasma involving particle interactions with the electromagnetic field. In general, the fluid simulation consumes comparatively less computational resources but the result is approximate. The kinetic simulation is opposite. But this simple distinction between fluid and kinetic simulations is becoming more complex through the emergence of hybrid codes that are the combinations between those two simulations and have mixture features of them. For the simulation of energetic particle driven instabilities, hybrid codes are often used. Several hybrid simulation models have been constructed [20, 21, 22, 23, 13] to study the evolution of Alfvén eigenmodes and EGAM. The thermal plasmas are treated as fluids, while the energetic particles described by kinetic equations. The thermal plasmas and energetic particles are usually coupled together by the current density or by the pressure.

MEGA code is used in the present thesis.[17, 18, 10] It is a hybrid code
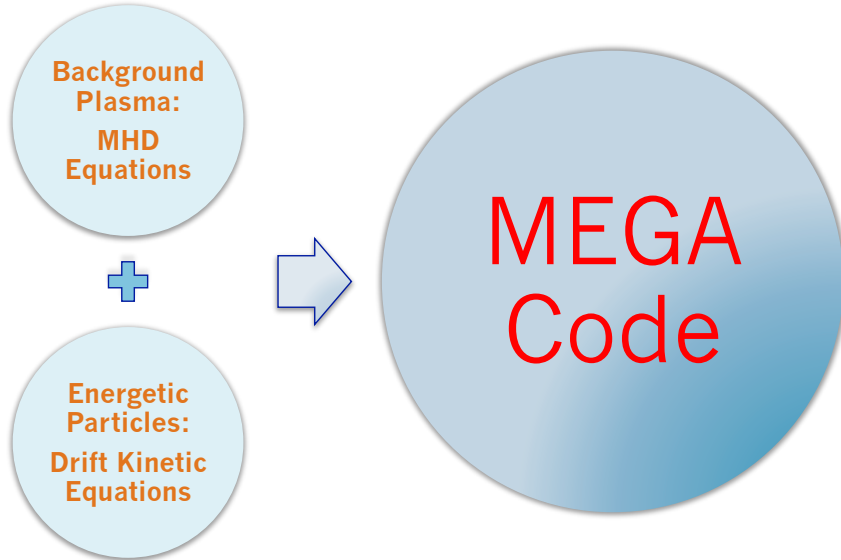
Figure 2.2: Schematic diagram of MEGA code.

and the model is portrayed briefly in Fig. 2.2. The background plasmas and the energetic particles are described by the ideal MHD equations and the drift kinetic equations, respectively. They are coupled by the current density. Various numerical schemes, for example, the particles in cell (PIC) method[19, 24, 25], δf method[26, 27, 28], the fourth order finite difference method[29, 30, 31], and the fourth order Runge-Kutta method[32, 29, 30, 31] are implemented in MEGA.

2.2 Basic equations

In the MEGA code, the bulk plasma is described by the nonlinear MHD equations and the energetic ions are simulated with the δf particle method [26, 27, 28]. The MHD equations with the energetic ion effects are given by

$$\frac{\partial \rho}{\partial t} = -\nabla \cdot (\rho \mathbf{v}) + \nu_n \triangle (\rho - \rho_{eq}), \tag{2.1}$$

$$\rho\frac{\partial}{\partial t}\mathbf{v} = -\rho\boldsymbol{\omega}\times\mathbf{v} - \rho\nabla(\frac{v^2}{2}) - \nabla p + (\mathbf{j} - \mathbf{j}'_h)\times\mathbf{B}$$
$$-\nabla\times(\nu\rho\boldsymbol{\omega}) + \frac{4}{3}\nabla(\nu\rho\nabla\cdot\mathbf{v}), \tag{2.2}$$

$$\frac{\partial\mathbf{B}}{\partial t} = -\nabla\times\mathbf{E}, \tag{2.3}$$

$$\frac{\partial p}{\partial t} = -\nabla\cdot(p\mathbf{v}) - (\gamma-1)p\nabla\cdot\mathbf{v} + (\gamma-1)$$
$$\times[\nu\rho\omega^2 + \frac{4}{3}\nu\rho(\nabla\cdot\mathbf{v})^2 + \eta\mathbf{j}\cdot(\mathbf{j}-\mathbf{j}_{eq})] + \nu_n\triangle(p-p_{eq}), \tag{2.4}$$

$$\mathbf{E} = -\mathbf{v}\times\mathbf{B} + \eta(\mathbf{j}-\mathbf{j}_{eq}), \tag{2.5}$$

$$\boldsymbol{\omega} = \boldsymbol{\nabla}\times\mathbf{v,} \tag{2.6}$$

$$\mathbf{j} = \frac{1}{\mu_0}\nabla\times\mathbf{B,} \tag{2.7}$$

where μ_0 is the vacuum magnetic permeability, γ is the adiabatic constant, ν and ν_n are artificial viscosity and diffusion coefficients chosen to maintain numerical stability and all the other quantities are conventional. The subscript 'eq' represents the equilibrium variables. The energetic ion contribution is included in the MHD momentum equation [Eq. (2.2)] as the energetic ion current density. The quantity $\mathbf{j}'_h$ is the energetic ion current density without $\mathbf{E}\times\mathbf{B}$ drift. We see that electromagnetic field is given by the standard MHD description. This model is accurate under the condition that the energetic ion density is much less than the bulk plasma density.

The MHD equations are solved using a fourth order (in both space and time) finite difference scheme. The energetic ion current density $\mathbf{j}'_h$ in Eq. (2.2) includes the contributions from parallel velocity, magnetic curvature and gradient drifts, and magnetization current. The $\mathbf{E}\times\mathbf{B}$ drift disappears in $\mathbf{j}'_h$ due to the quasi-neutrality [17]. The computational particles are initially loaded uniformly in the phase space.

The energetic particles are described by the drift-kinetic equations [33]. The guiding-center velocity $\mathbf{u}$ is given by

$$\mathbf{u} = \mathbf{v}^*_{\parallel} + \mathbf{v}_E + \mathbf{v}_B, \tag{2.8}$$

13

$$\mathbf{v}_\parallel^* = \frac{v_\parallel}{B^*}(\mathbf{B} + \rho_\parallel B \nabla \times \mathbf{b}), \tag{2.9}$$

$$\mathbf{v}_E = \frac{1}{B^*}(\mathbf{E} \times \mathbf{B}), \tag{2.10}$$

$$\mathbf{v}_B = \frac{1}{Z_h e B^*}(-\mu \nabla B \times \mathbf{b}), \tag{2.11}$$

$$\rho_\parallel = \frac{m_h v_\parallel}{Z_h e B}, \tag{2.12}$$

$$\mathbf{b} = \mathbf{B}/B, \tag{2.13}$$

$$B^* = B(1 + \rho_\parallel \mathbf{b} \cdot \nabla \times \mathbf{b}), \tag{2.14}$$

$$m_h v_\parallel \frac{dv_\parallel}{dt} = \mathbf{v}_\parallel^* \cdot (Z_h e \mathbf{E} - \mu \nabla B), \tag{2.15}$$

where $v_\parallel$ is the velocity parallel to the magnetic field, μ is the magnetic moment, m_h is energetic particle mass and $Z_h e$ is energetic particle charge. The energetic particle current density $\mathbf{j}'_h$ in Eq. (2.2) is

$$\mathbf{j}'_h = \int (\mathbf{v}_\parallel^* + \mathbf{v}_B) Z_h e f d^3 v - \nabla \times \int \mu \mathbf{b} f d^3 v, \tag{2.16}$$

and $\mathbf{v}_E$ doesn't appear because of the quasi-neutrality [17].

The δf particle method is applied for the energetic particles[26, 27, 28]. The equilibrium energetic particle distribution f_0 can be written as

$$f_0 = f_0(P_\phi, v, \mu, \sigma), \tag{2.17}$$

$$P_\phi = Z_h e \psi + R m_h v_\parallel \frac{B_\phi}{B}, \tag{2.18}$$

where P_ϕ is the toroidal canonical momentum, Z_h is the effective charge of the energetic particle, e is the elementary charge, ψ is the poloidal magnetic flux, R is the particle major radius, v is the total velocity, B_ϕ is the magnetic field strength in ϕ direction, B is the magnetic field strength, and μ is the magnetic moment. The variable σ takes the values, $\sigma = -1$ for passing particles with $v_\parallel < 0$, $\sigma = 0$ for trapped particles, and $\sigma = 1$ for passing particles with $v_\parallel > 0$. The marker particles are initially loaded uniformly in the phase

14

space and the number of energetic ions that each marker particle represents is in proportion to the initial distribution function. A normalization factor α is introduced to initially satisfy

$$\int P_{h\parallel} dV = \alpha \sum_{i=1}^{N} m_h v_\parallel^2 f_0(P_\phi, v, \mu), \tag{2.19}$$

where $P_{h\parallel}$ is the parallel pressure of energetic particles and N is the total number of marker particles used. The time evolution of the weight of the i-th particle is described by

$$\frac{dw_i}{dt} = -\alpha \left(\frac{dP_\phi}{dt} \frac{\partial f_0}{\partial P_\phi} + \frac{dv}{dt} \frac{\partial f_0}{\partial v} \right)_{\mathbf{x}=\mathbf{x}_i, \mathbf{v}=\mathbf{v}_i} \tag{2.20}$$

and the initial condition is $w_i|_{t=0} = 0$. Using this weight, the energetic particle current $\mathbf{j}_h'$ in Eq.(2.2) and Eq.(2.16) can be written as

$$\mathbf{j}_h' = \mathbf{j}_{h0} + \sum_{i=1}^{N} w_i Z_h e(\mathbf{v}_{\parallel i}^* + \mathbf{v}_{Bi}) S(\mathbf{x} - \mathbf{x}_i) - \nabla \times \left[\mathbf{b} \sum_{i=1}^{N} w_i \mu_i S(\mathbf{x} - \mathbf{x}_i) \right], \tag{2.21}$$

where $S(\mathbf{x} - \mathbf{x}_i)$ is the shape factor of the marker particle and $\mathbf{j}_{h0}$ is the energetic particle current density in the equilibrium.

2.3   Computational methods

The energetic particles are simulated by PIC method.[19, 24, 25] In MEGA code, the particle motion is described by Eq. (2.15), and the field is included in MHD equations. One super particle contains N real particles and these real particles move together. In the present simulations, the order of magnitude of N is 1×10^{11}. Spatial grids are meshed. The field strength is not calculated continuously but discretely on the grid points. On the other hand, particle positions are continuous. At the beginning of simulation, particles
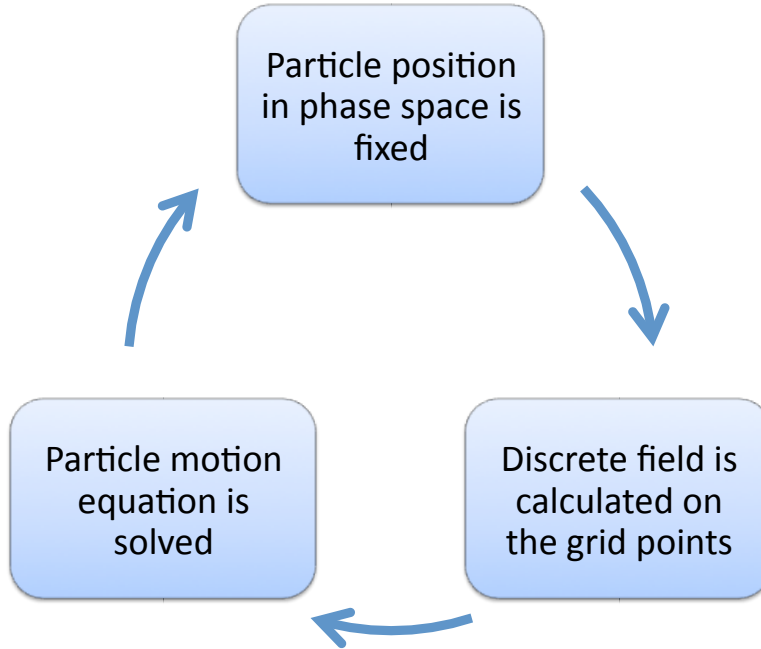
Figure 2.3: The PIC cycle in MEGA code.

are loaded into the phase space randomly. Then, the discrete field on the grids is calculated. Based on the field, the equation of motion is solved. Then, new positions of particles in phase space at the next time step are fixed. This process is illustrated in Fig. 2.3.

The δf method is also applied for the energetic particles.[26, 27, 28] Before the δf method was developed, usual particle simulations were based on the importance sampling Monte Carlo technique, where the computational particles are assumed to have the same distribution in phase space as the physical particles in the problem being investigated. This technique suffered from noise problems. The δf method is based on the control variates Monte Carlo technique. Assume that there exists a function f_0 which satisfies 2 conditions: (i) the analytical form of f_0 can be found and (ii) $||f - f_0||/f \ll 1$. Then the noise can be reduced by applying a Monte Carlo technique only to the δf part (or the $f - f_0$ part). Notice that the low noise is different with high

16

accuracy. In the δf method, the noise can be low if a good control variate f_0 is chosen, while the high accuracy can be realized with large number of particles.

The spatial derivatives in equations are approximately calculated by using the finite difference method.[29, 30, 31] To obtain higher accuracy, the higher order of the finite difference approximation is required, and more computational resources are consumed. All things considered, the 4th order finite difference approximation is applied in the present thesis. The 1st order spatial derivative of a variable f at the i-th grid point is represented as

$$f_i^{(1)} = \frac{1}{12h}(-f_{i+2} + 8f_{i+1} - 8f_{i-1} + f_{i-2}), \tag{2.22}$$

where subscripts are the indexes of the numerical grids and h is the grid size. The numerical error of Eq. (2.22) is of the order of h^4 at most. It is good enough and the consumption of computational resources is also acceptable.

The Runge-Kutta method is applied for time integration.[32, 29, 30, 31] Similar with the cases of finite difference, the 4th order Runge-Kutta method is used in the present thesis to keep balance between accuracy and resources consumption. Denote the independent variables (ρ,$\mathbf{v}$,$\mathbf{B}$, and p) by the vector $\mathbf{y}$, and the sum of the right hand side of Eq. (2.1)-(2.4) by the vector $\mathbf{g}$, then we can write the 4th order Runge-Kutta method as follows:

$$\mathbf{y}^{n+1} = \mathbf{y}^n + \frac{1}{6}(\mathbf{k}_1 + 2\mathbf{k}_2 + 2\mathbf{k}_3 + \mathbf{k}_4), \tag{2.23}$$

$$\mathbf{k}_1 = \Delta t \mathbf{g}(\mathbf{y}^n), \tag{2.24}$$

$$\mathbf{k}_2 = \Delta t \mathbf{g}(\mathbf{y}^n + \frac{1}{2}\mathbf{k}_1), \tag{2.25}$$

$$\mathbf{k}_3 = \Delta t \mathbf{g}(\mathbf{y}^n + \frac{1}{2}\mathbf{k}_2), \tag{2.26}$$

$$\mathbf{k}_4 = \Delta t \mathbf{g}(\mathbf{y}^n + \mathbf{k}_3), \tag{2.27}$$

where superscripts are the temporal indexes and Δt is the time step width. The numerical error is of the order of $(\Delta t)^5$ at most.

2.4 Geometry, normalization, and parameters

The cylindrical coordinates (R, ϕ, z) is used, where R is the major radius coordinate, ϕ is the toroidal angle coordinate and z is the vertical coordinate. The simulation region in R and z coordinates is $R_0 - a \leq R \leq R_0 + a$ and $-a \leq z \leq a$, where R_0 is the major radius and a is the minor radius. The range of ϕ is decided by the toroidal mode number n, and the details will be mentioned in chapter 3 and 4. The outermost magnetic surface is circular.

In this simulation, time is normalized by the Larmor period of energetic particles, Ω_h^{-1}, and velocity is normalized by the Alfvén velocity v_A, then length is normalized by v_A/Ω_h. The magnetic field strength at the magnetic axis is set to be unity, that means $B_0 = 1$. In addition, $m_h = 1$ and $\mu_0 = 1$. The pressure is normalized by B_0^2/μ_0 while the beta value is defined by $\beta = 2\mu_0 P/B_0^2$.

The detailed simulation parameters will be described in chapter 3 and 4. Notice the time step width is limited by the Courant condition (also named as Courant-Friedrichs-Lewy condition or abbreviated to CFL condition):[30, 25]

$$\Delta t \leq \alpha \Delta x/v_0, \tag{2.28}$$

$$\alpha \sim O(1), \tag{2.29}$$

where α is a constant of order of unity and the exact value depends on the numerical scheme, Δx is the grid size, and v_0 is the wave propagation speed. In the present simulation, the range of α is between 0.61 and 0.94, and it takes different values for different cases.

2.5 Computer resources consumption

The numerical computations are performed at the Plasma Simulator (Hitachi SR16000) of the National Institute for Fusion Science. This machine is composed of 128 nodes. It achieved a speed of 56.65 teraflops for the Top 500 list and has a peak performance of 77.00 teraflops. The computer resources for Alfvén eigenmodes and EGAM are different. In general, 2 nodes are used for 10 hours for Alfvén eigenmodes simulation, and 16 nodes are used for 50 hours for EGAM simulation. The typical memory consumptions are $\sim 4GB$ and $\sim 60GB$ for Alfvén eigenmodes and EGAM, respectively. Notice that the computer resources consumption changes with many factors, for example, the number of grid points, the number of particles, and the specific physical model and parameters. For Alfvén eigenmodes case, normally the simulation is terminated before $1.5t_s$, where t_s represents the time of the saturation of the instability. For EGAM case, the details of nonlinear frequency chirping needs to be investigated, so the simulation is terminated after $3t_s$. In addition, the evolution of distribution function is studied carefully, so more particles are used for EGAM simulation.

Chapter 3

Interaction between Energetic Particles and Alfvén Eingemodes in Reversed Shear Plasmas

3.1 Introduction of Alfvén eigenmodes

Alfvén eigenmodes accompanied by frequency chirping due to the plasma equilibrium evolution were observed in many tokamaks [34, 35, 36, 37, 38, 39, 40] and helical devices [41, 42]. This type of Alfvén eigenmodes has been identified as the reversed shear Alfvén eigenmode (RSAE mode), which was discovered by the numerical analysis using the TASK/WM code [43, 44]. The spatial profile of RSAE mode peaks at the location of the minimum safety factor value for tokamaks and at the maximum for helical devices. It was demonstrated that the equilibrium evolution of reversed shear plasmas leads to the frequency chirping of RSAE modes and the transition between the RSAE modes and

the toroidal Alfvén eigenmodes (TAE modes) [45, 46]. It has been clarified that the RSAE modes (or sometimes called Alfvén cascade modes) can be described in the purely magnetohydrodynamics framework without energetic particle effects [47], although the energetic particles can potentially play an essential role for the existence of the Alfvén modes in reversed shear plasmas [48, 49]. The effect of the plasma compressibility on the lowest frequency of the RSAE modes was studied theoretically [50, 51]. Furthermore, the damping rate for RSAE modes and TAE modes was numerically analyzed using the TASK/WM code [52, 36].

Although a large number of studies have been made on the frequency evolution of RSAE modes, little attention has been paid to the interaction between energetic particles and RSAE modes. An important question for fusion burning plasmas is whether the energetic particle transport changes or not when the transition between RSAE modes and TAE modes takes place. In order to answer this question, we have investigated the interaction of energetic particles with RSAE modes or TAE modes using the MEGA code [17, 53, 18], a hybrid simulation code for magnetohydrodynamics (MHD) and energetic particles. We focus on the difference in energetic particle transport between RSAE modes and TAE modes. When the energetic particle distribution is isotropic in velocity space, we have found that the energetic particles both co- and counter-going are transported by the TAE modes, whereas only the co-going particles are transported by the RSAE modes. The growth rate takes the minimum value just before the transition from RSAE mode to TAE mode. The reason for these results are examined by complementary simulations using purely co- or counter-going energetic particles.

This chapter is organized as follows. In Section 3.2, the simulation model and computational method are described. In Section 3.3, the simulation results of RSAE modes and TAE modes are shown, and the differences in

the energetic particle transport between the two types of eigenmodes are discussed. Numerical convergence in number of computational particles and time step width is also examined. Section 3.4 is devoted to summary.

3.2 Simulation parameters

3.2.1 Energetic particle distribution

The cylindrical coordinates (R, ϕ, z) is used, where R is the major radius coordinate, ϕ is the toroidal angle coordinate and z is the vertical coordinate. In this work, the energetic particle beta profile is

$$\beta_h(x) = \beta_{h0} e^{-(x/\xi)^2}, \tag{3.1}$$

where β_h is the ratio of the energetic particle pressure and the magnetic pressure, $x = r/a$, r is the minor radius coordinate, a is the plasma minor radius, β_{h0} is the energetic particle beta value at the magnetic axis. The parameter ξ is a normalized spatial scale length and set to be 0.4.

The equilibrium energetic particle distribution f_0 can be written as

$$f_0 = f_0(P_\phi, v, \mu, \sigma), \tag{3.2}$$

where P_ϕ is the toroidal canonical momentum, v is the total velocity, and μ is the magnetic moment. The variable σ takes the values, $\sigma = -1$ for passing particles with $v_\parallel < 0$, $\sigma = 0$ for trapped particles, and $\sigma = 1$ for passing particles with $v_\parallel > 0$. The equilibrium distribution function f_0 is expanded in a power series of $\tilde{\psi}$ to fit the energetic particle beta profile, where $\tilde{\psi}$ is defined by

$$\tilde{\psi} = \left(P_\phi - \sigma m_h R b_\phi \sqrt{v^2 - 2\mu B_{min}/m_h} \right) /Z_h e \tag{3.3}$$

where B_{min} is the minimum value of the magnetic field strength in the simulation domain. In this work, a normalization factor α is introduced to satisfy

$$\int \frac{1}{2} \left(P_{h\parallel} + 2P_{h\perp} \right) dV = \alpha \sum_{i=1}^{N} \left(\frac{1}{2} m_h v_\parallel^2 + \mu_i B(\mathbf{x}_i)^2 \right) f_0(P_{\phi_i}, v_i, \mu_i, \sigma_i),$$

$$(3.4)$$

where $P_{h\parallel}$ and $P_{h\perp}$ are the energetic particle parallel and perpendicular pressures and N is the total number of marker particles used.

3.2.2 Simulation settings

We focus on $n = 4$ Alfvén eigenmodes, which are exact solutions of the equations of a quarter of the tokamak domain with the toroidal angle taken from $0 \leq \phi \leq \frac{\pi}{2}$. Then, the simulation region is $R_c - a \leq R_c \leq R_c + a, 0 \leq \phi \leq \frac{\pi}{2}$ and $-a \leq z \leq a$, where R_c is the major radius. The outermost magnetic surface is circular with aspect ratio $R_c/a = 3.0$. The number of marker particles is 5.24×10^5, but a larger particle number is also used to investigate the numerical convergence. The number of grid points is $100 \times 16 \times 100$ for the cylindrical coordinates (R, ϕ, z). The viscosity and diffusivity are set to be $\nu = \nu_n = 10^{-6} v_A R_c$ and the resistivity $\eta = 10^{-6} \mu_0 v_A R_c$ in the simulation, where v_A is the Alfvén speed. Different energetic particle slowing-down distribution functions, i) slowing-down distribution which is isotropic in velocity space, ii) slowing-down distribution with only co-passing particles, and iii) slowing-down distribution with only counter-passing particles, are applied to study the differences between RSAE modes and TAE modes.

3.2.3   Non-Monotonic Safety Factor Profiles

In this chapter, non-monotonic safety factor profiles (q profiles) are used to simulate both RSAE modes and TAE modes. The q profile is presented as

$$q(r) = q_{min} + C_1(r^2 - r_{min}^2)^2 + C_2(r^2 - r_{min}^2)^3, \qquad (3.5)$$

$$C_1 = \frac{C_I}{r_{min}^8 - 2r_{min}^6 + r_{min}^4} \qquad (3.6)$$

$$C_I = -(q_0 - q_a)r_{min}^6 + (3q_{min} - 3q_0)r_{min}^4$$
$$+ (3q_0 - 3q_{min})r_{min}^2 + q_{min} - q_0 \qquad (3.7)$$

$$C_2 = \frac{C_{II}}{r_{min}^8 - 2r_{min}^6 + r_{min}^4} \qquad (3.8)$$

$$C_{II} = (q_0 - q_a)r_{min}^4 + (2q_{min} - 2q_0)r_{min}^2 - q_{min} + q_0 \qquad (3.9)$$

where q_0 is the q value on the magnetic axis, q_a is the q value on the plasma edge, q_{min} is the minimum value of the safety factor and r_{min} is the radial position of q_{min}. In this chapter, the parameters q_0, q_a, and r_{min} are set to be $q_0 = 2.0$, $q_a = 3.0$, and $r_{min} = 0.433$, respectively.

3.3   Simulation results

3.3.1   Isotropic slowing-down distribution

In this subsection, the evolution of Alfvén eigenmodes for different q_{min} values is investigated. The slowing-down distribution of energetic particles is isotropic in velocity space with the maximum velocity $1.7v_A$ and the critical velocity $0.5v_A$. The central energetic particle beta value is $\beta_{h0} = 1.0\%$. The ratio of the minor radius to the Alfvénic Larmor radius is $a\Omega_h/v_A = 20$. The spatial profiles, frequency, and evolution of the Alfvén eigenmodes, and the energetic particle transport are compared. The shear Alfvén continua and

the mode spatial profiles are shown in Fig. 3.1 for $q_{min} = 1.95$ and 1.875. We see in the figure the continuum gaps at $r = r_{min} = 0.433$ for both $q_{min} = 1.95$ and $q_{min} = 1.875$. The gap for $q_{min} = 1.95$ is created by the reversed shear, while the gap for $q_{min} = 1.875$ is a TAE gap created by toroidicity.[1] The spatial profiles of the Alfvén eigenmodes are also compared in this figure. For $q_{min} = 1.95$, we see only one dominant poloidal harmonic $m = 8$, while for $q_{min} = 1.875$ two poloidal harmonics $m = 7$ and 8 are dominant. These profiles indicate that they are an RSAE mode for $q_{min} = 1.95$ and a TAE mode for $q_{min} = 1.875$. The modes are also plotted on poloidal cross section as shown in Fig. 3.2. This figure shows the mode amplitude E_ϕ, and the two panels share the same vertical axis. It is easy to figure out RSAE poloidal mode number because the mode strength is similar everywhere. But it is not so easy to figure out TAE poloidal mode number because the mode is weak in high field side but strong in low field side. It is caused by the coupling between $m = 7$ and $m = 8$ modes.

The time evolutions of the RSAE mode and the TAE mode are shown in Fig. 3.3. The mode linear growth rate and saturation level are higher for the RSAE mode than for the TAE mode. The frequency is $0.17\omega_A$ and $0.25\omega_A$ for the RSAE mode and the TAE mode, respectively.

The mode frequency and growth rate for different q_{min} are shown in Fig. 3.4. For $q_{min} \leq 1.875$, the TAE gap is created and the destabilized modes are TAE modes. For $q_{min} > 1.875$, the destabilized modes are RSAE modes. The frequency of the RSAE modes chirps up to the TAE frequency as q_{min} reduces from 1.975 to 1.875. This qualitatively reproduces the frequency up-shift observed in the tokamak experiments [34, 35, 37, 38, 40]. In the case of $q_{min} = 1.975$, the RSAE frequency $\omega_{RSAE} = 0.15\omega_A$, which is higher than the geodesic acoustic mode (GAM) frequency $\omega_{GAM} = 0.11\omega_A$ and much

---

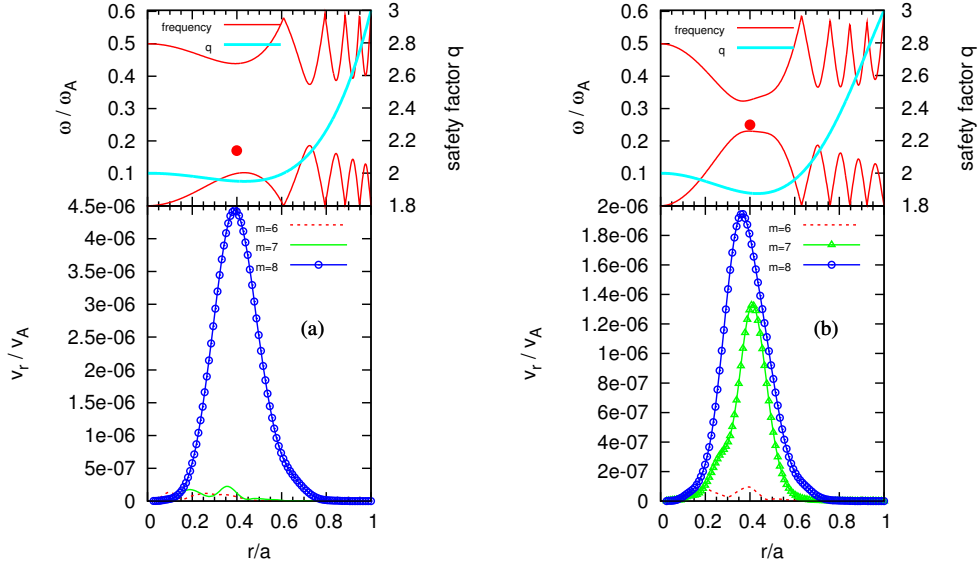[1]For detailed explaination, please read appendix A.

Figure 3.1: Shear Alfvén continua, safety factor profiles, and spatial profiles of Alfvén eigenmodes for (a) $q_{min} = 1.95$ (RSAE mode) and for (b) $q_{min} = 1.875$ (TAE mode) with toroidal mode number $n = 4$. The closed circles in upper panels represent the mode peak locations and the mode frequencies, (a) $0.17\omega_A$ and (b)$0.25\omega_A$.
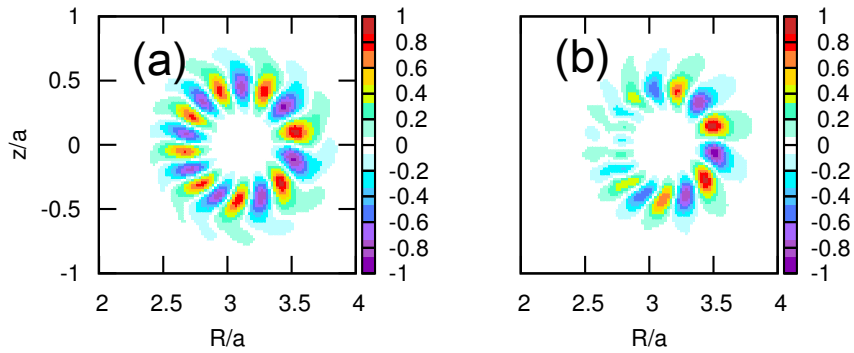

Figure 3.2: The mode amplitude E_ϕ of (a) RSAE and (b) TAE on poloidal cross section. These 2 panels share the same vertical axis.
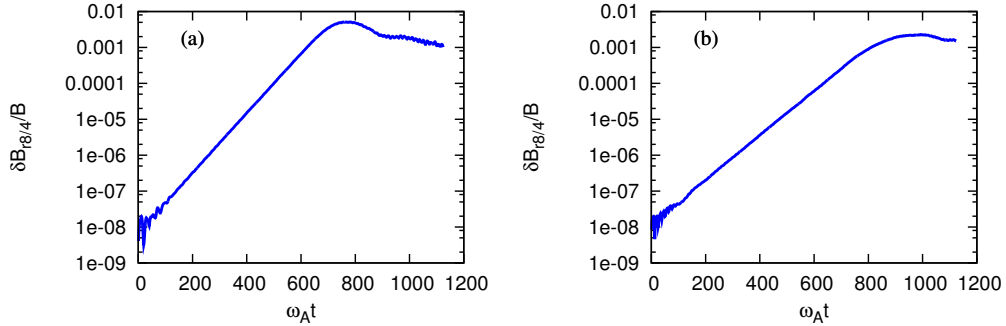
Figure 3.3: Amplitude evolutions of (a) RSAE mode and (b) TAE mode.

higher than the shear Alfvén continuum frequency $0.05\omega_A$. The growth rate of the Alfvén eigenmodes are also shown in Fig. 3.4. As q_{min} decreases from 1.95 to 1.90, the growth rate decreases and takes the minimum value around $q_{min} = 1.90$. The growth rate rises up as q_{min} decreases from 1.90 to 1.825. The decrease in growth rate from $q_{min} = 1.95$ to 1.90 may partially arise from the increase in frequency because theory predicts [54] that the energetic particle drive γ_L depends on the mode frequency ω by

$$\gamma_L \simeq \frac{9}{4}\beta_h(\omega_{*h} - \frac{1}{2}\omega)F(v_A/v_h) \ , \tag{3.10}$$

$$F(x) = x(1 + 2x^2 + 2x^4)e^{-x^2} \ , \tag{3.11}$$

where v_h is the velocity that represents the average energy of the slowing down distribution.

When q_{min} reaches down to 1.875, the transition from RSAE mode to TAE mode takes place as is shown in Fig. 3.1. The emergence of second dominant poloidal harmonic $m = 7$ adds a new branch of energy transfer from the energetic particles to the Alfvén eigenmodes. This may lead to the increase in growth rate from $q_{min} = 1.90$ to 1.825. For the purpose of the clarification of this point, we investigate the energetic particle transport and the cases with only co-passing particles or with only counter-passing particles in the following subsections.
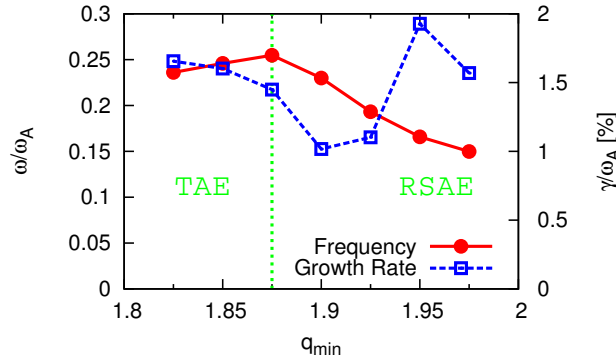
27

Figure 3.4: Mode frequency and growth rates v.s. q_{min}. The straight vertical dotted line ($q_{min} = 1.875$) represents the boundary between TAE modes and RSAE modes.

3.3.2 Energetic particle transport

The energetic particle pressure profiles in the saturated phases are plotted as functions of normalized minor radius in Fig. 3.5. We see the decrease in the energetic particle pressure in the saturated phase. This indicates the energetic particles are transported by the Alfvén eigenmodes.[1] In addition, the relation between transport and growth rate can also be found in Fig. 3.5. For the $q_{min} = 1.95$ RSAE mode case, the growth rate is higher and the pressure is modified more than all the other cases. By contrast, for the $q_{min} = 1.90$ RSAE mode case, the growth rate is lowest and the pressure reduction is the smallest. Then, the transport has a correlation to the mode growth rate. The energetic particle density re-distributions are similar to the pressure re-distributions.

We can see the most important difference between RSAE and TAE modes in energetic particle transport. The density perturbations of energetic parti-

---

[1]Particles can be transported far because of the wide orbit width. The details are illustrated in Appendix B.
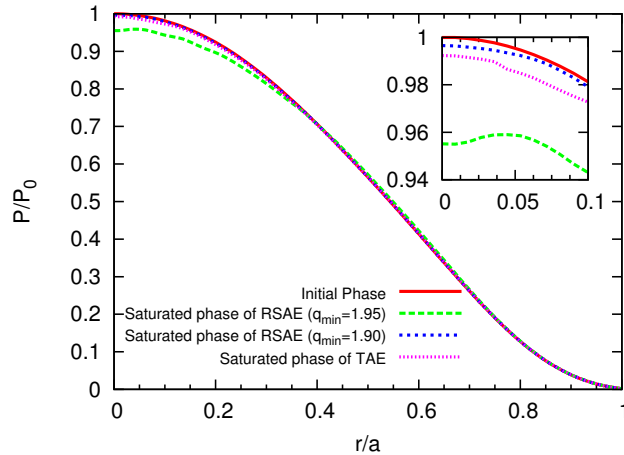
Figure 3.5: The energetic particle pressure profiles in the saturated phases at $\omega_A t = 1042$.

cles due to the RSAE and TAE modes are plotted on a poloidal cross section in Fig. 3.6. Figure 3.6 (a) and (b) show the density perturbation of co-going particles and counter-going particles, respectively, due to the RSAE mode. We see a clear density perturbation in (a). However, it is not clear in (b), and the different colors seem to be distributed randomly because of very weak perturbation. Figure 3.6 (c) and (d) show those due to the TAE mode. We see a weak density perturbation in (d), but it is not so weak as that in Fig. (b). So, for the RSAE mode, the energetic particles co-going to the plasma current are primarily transported, whereas both the co- and counter-going particles are transported by the TAE mode.

3.3.3 Interaction with co- or counter-passing particles

As shown above, both the co- and counter-going particles are transported by the TAE mode, whereas the co-going particles are primarily transported by the RSAE mode. In order to clarify the role of the counter-going particles, two kinds of energetic particle distribution functions, slowing-down distribu-

29
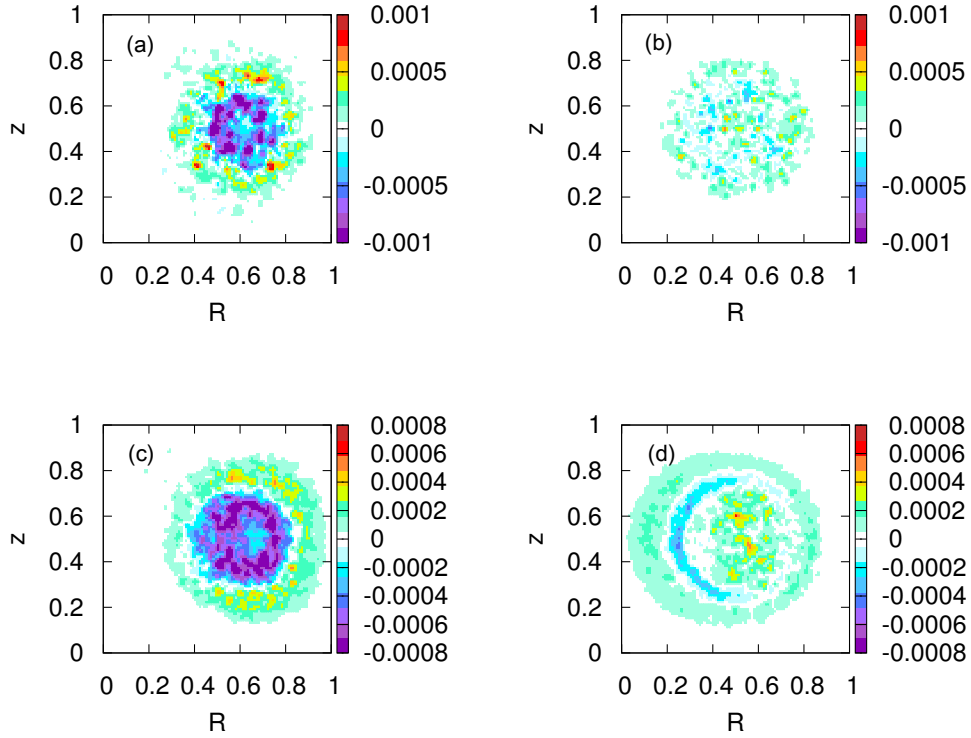
Figure 3.6: Density perturbation on a poloidal cross section of (a) co-going particles due to RSAE, (b) counter-going particles due to RSAE, (c) co-going particles due to TAE, and (d) counter-going particles due to TAE. The horizontal and vertical axes are normalized by $2a$ where a is the plasma minor radius. The range of the horizontal axis corresponds to $R_0 - a \leq R \leq R_0 + a$. The q_{min} value for the RSAE and the TAE cases are 1.95 and 1.825, respectively.

tions with only co-passing particles and with only counter-passing particles, are investigated in this subsection.

The spatial profiles of the destabilized RSAE modes are shown in Fig. 3.7. The central energetic particle beta value is $\beta_{h0} = 0.5\%$ and the minimum safety factor value is $q_{min} = 1.95$. The primary poloidal mode number and the frequency are $m = 8$ and $0.17\omega_A$ for the co-passing particles, while they are $m = 7$ and $0.38\omega_A$ for the counter-passing particles. These results indicate that the co-passing particles interact with poloidal harmonic $m = 8$ while the counter-passing particles interact with $m = 7$. This clearly explains why the RSAE modes of the primary poloidal harmonic $m = 8$ transport the co-going particles, whereas the TAE modes of the dominant poloidal harmonics $m = 7$ and 8 transport both the co- and counter-going particles. In a JT-60U experiment, both high-frequency and low-frequency RSAE modes were observed with the co-beam injection.[36] It is important to point out the fact that both high-frequency RSAE mode and low-frequency mode exist for the co-passing particle case, although the former is very weak. The frequency spectrum with $q_{min} = 1.95$ is shown in Fig. 3.8, the ratio of high-frequency $(0.42\omega_A)$ RSAE mode amplitude to low-frequency $(0.18\omega_A)$ one is about 1:22. It is so weak that only the low-frequency RSAE mode profile is shown in the present work.

The frequency and growth rate for the co-passing particles and the counter-passing particles are shown in Fig. 3.9 for different q_{min}. The central energetic particle beta values are chosen so that the growth rate for $q_{min} = 1.95$ is close to that for the isotropic slowing-down distribution shown in Fig. 3.4, and are $\beta_{h0} = 0.39\%$ for the co-passing particles and $\beta_{h0} = 0.75\%$ for the counter-passing particles. The velocity of energetic particles are $1.2v_A$. For the counter-passing particles, the continuous frequency drop of the RSAE modes which can be expected when q_{min} decreases does not take place. We
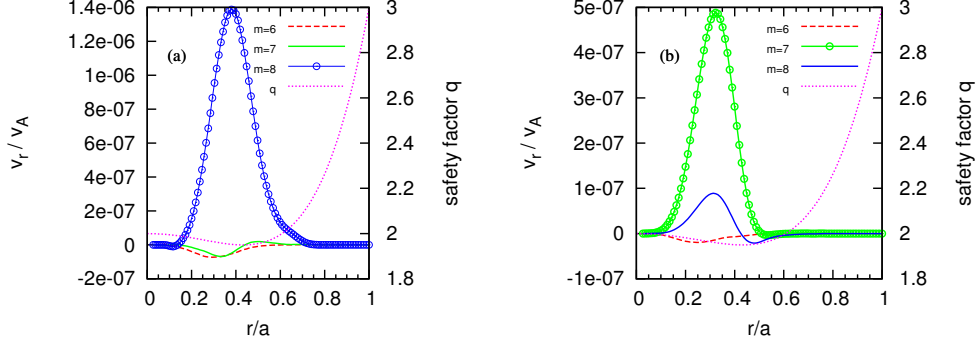
Figure 3.7: Spatial profiles of $n = 4$ RSAE modes with $q_{min} = 1.95$ for (a) co-passing particles and (b) counter-passing particles. The primary poloidal harmonic is $m = 8$ for co-passing particles, (a); while $m = 7$ harmonic is dominant for counter-passing particles, (b).

Figure 3.8: Frequency spectrum with $q_{min} = 1.95$ for co-passing particles. One mode peaks around $0.18\omega_A$ and another mode peaks around $0.42\omega_A$. They correspond to low-frequency RSAE mode and high-frequency RSAE mode, respectively.

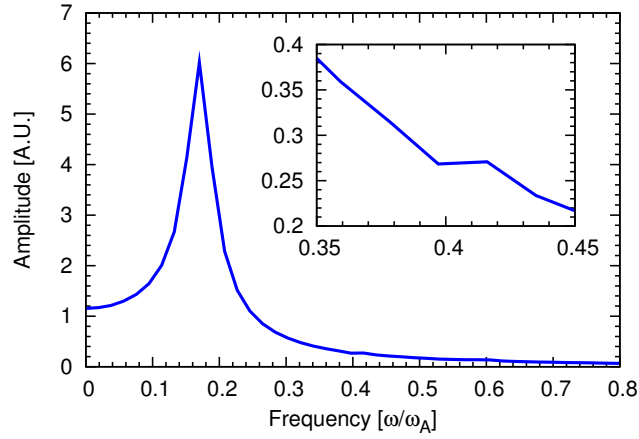can see in Fig. 3.9 that Alfvén eigenmodes are stable for $q_{min} < 1.9$ except for $q_{min} = 1.825$ for the counter-passing particles. The mode spatial profile and the shear Alfvén continua for the counter-passing particle case with $q_{min} = 1.825$ are shown in Fig. 3.10. We see in the figure that the mode has only one dominant poloidal harmonic $m = 7$, and the spatial profile peaks around the location of the minimum safety factor value. The frequency $0.18\omega_A$ is also close to the Alfvén continuum frequency at the minimum safety factor value. The frequency of the mode intersects with the shear Alfvén continuum, but the continuum damping is not critically strong because the magnetic shear is weak.[55, 56] Then, the unstable mode is an RSAE mode and not a TAE mode. No TAE mode is destabilized for either the co-passing or the counter-passing particles. These results are contrastive to the results for the isotropic slowing-down distribution. For the isotropic velocity distribution, the RSAE modes are destabilized by the co-going particles and the growth rate decreases as the RSAE mode frequency rises up. After the transition from RSAE modes to TAE modes, the counter-going particles contribute to the growth of the TAE modes through the interaction with $m = 7$ poloidal harmonic of the TAE modes.

3.3.4   Convergence studies

In order to confirm the simulation results, numerical convergences have been investigated with regard to the number of particles and the time step width. Different particle numbers and different time step widths are tested, and the time evolutions of the mode amplitudes overlap between each other, as shown in Fig. 3.11. Obviously, the growth rate and the saturation level are independent of the particle number and the time step width in these simulations. Therefore, the numerical convergence is good enough for the results presented in this chapter.
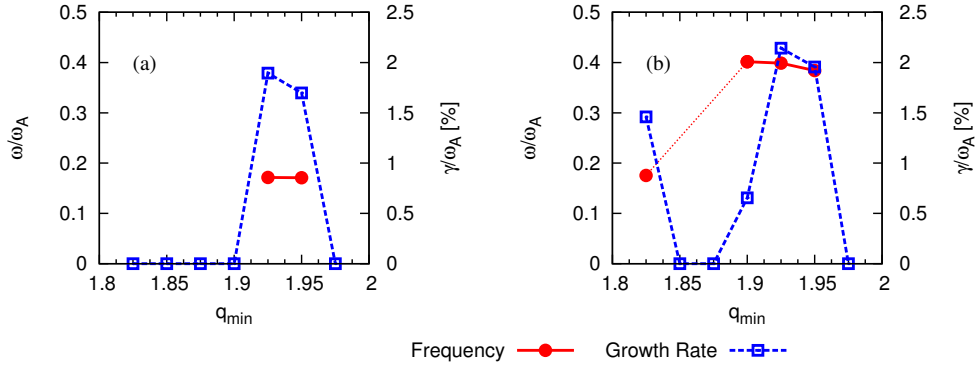
Figure 3.9: Alfvén eigenmode frequency and growth rate for (a) co-passing case with $\beta_{h0} = 0.39\%$ and (b) counter-passing case with $\beta_{h0} = 0.75\%$. The velocity of energetic particles are $1.2v_A$. For counter-passing particles, high-frequency RSAEs are excited for $q_{min} \geq 1.90$, and low-frequency RSAE is excited for $q_{min} = 1.825$.

Figure 3.10: Shear Alfvén continuum, safety factor profile, and spatial profile of Alfvén eigenmode for counter-passing particles with $q_{min} = 1.825$ and toroidal mode number $n = 4$. The closed circle in upper panel represents that the mode peaks around $r = r_{min}$ and mode frequency is $0.18\omega_A$.

34

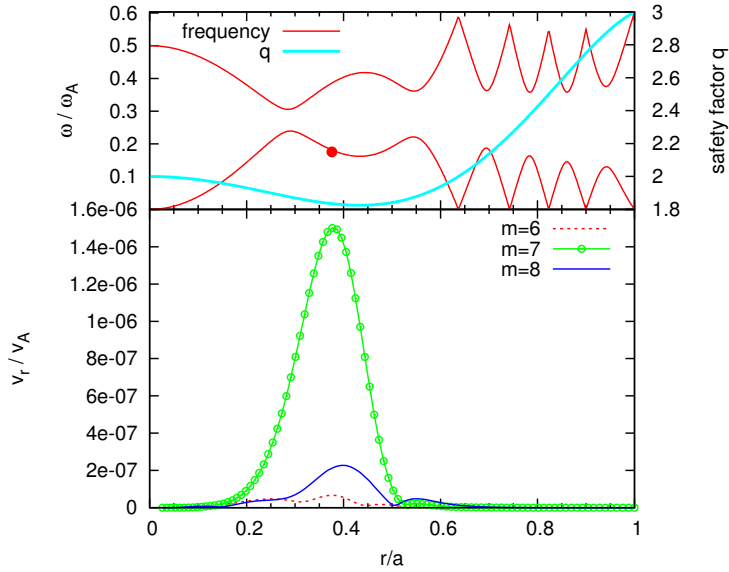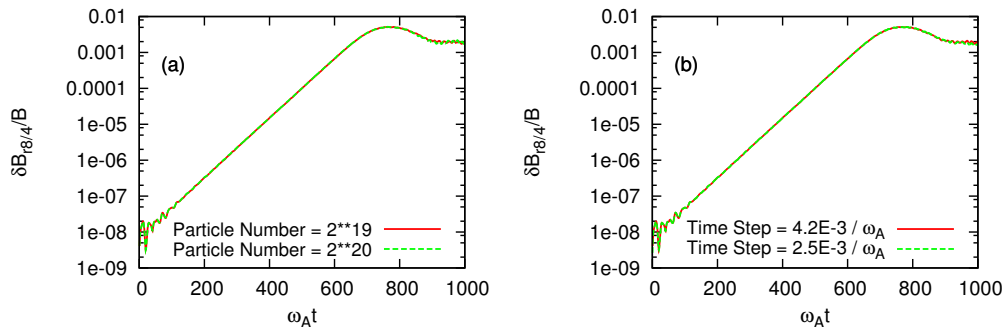Figure 3.11: Time evolution of the mode amplitude for (a) different numbers of particles and (b) different time step width. In panel (a), the total number particles used in the dashed curve is two times larger than that used in the solid one. In panel (b), the time step width used in the dashed curve is approximately half of that used in the solid one.

3.4 Summary

Alfvén eigenmodes are important issues in current fusion science and technology. We have investigated in this thesis the interaction between energetic particles and Alfvén eigenmodes in reversed shear tokamak plasmas using a hybrid simulation code for MHD and energetic particles, MEGA. The behaviors of RSAE and TAE modes in reversed shear configuration have been compared carefully. When the energetic particle distribution is isotropic in velocity space, the transition from low-frequency RSAE mode to TAE mode was demonstrated as the minimum safety-factor value decreases. The frequency rises up from a level above the geodesic acoustic mode frequency to the TAE frequency. It was found that the energetic particles both co- and counter-going to the plasma current are transported by the TAE mode, whereas the co-going particles are primarily transported by the low-frequency RSAE mode.

In order to acquire the better understanding of the role of the co- and

counter-going particles, the additional runs were performed with only co- or only counter-passing particles. It was found that when only the co-passing particles are retained, the low-frequency RSAE modes are destabilized. On the other hand, the high-frequency RSAE modes are destabilized when only the counter-passing particles are retained. In the purely co-passing and the purely counter-passing particle cases, no TAE mode was destabilized for the low q_{min} values. This is different from the isotropic velocity distribution case where the TAE modes are destabilized for the low q_{min} values, although the energetic particle beta values for the co-passing and the counter-passing particle cases are chosen so that the growth rate for $q_{min} = 1.95$ is close to that for the isotropic velocity distribution case. This difference arises from the fact that for the isotropic velocity distribution, the TAE modes are destabilized by both the co-going and the counter-going particles while the low-frequency RSAE modes are primarily destabilized by the co-going particles.

It is interesting to note that no TAE mode was observed for either the purely co-passing particle case or the purely counter-passing particle case. We can conclude that the RSAE modes are easier to destabilize than the TAE modes for such unbalanced beam-type distributions. Another interesting discovery is the high-frequency RSAE mode evolution in the purely counter-passing particle cases. The frequency is kept roughly constant as q_{min} decreases before the TAE gap is created. After the TAE gap is created as q_{min} decreases, the unstable mode is now a low-frequency RSAE mode whose poloidal mode number is kept the same as that for the greater q_{min} values. The continuous drop in frequency, which is expected to chirp from the high-frequency shear Alfvén continuum frequency to the TAE frequency, does not take place in the present simulation results.

Chapter 4

Linear properties and nonlinear evolution of Energetic Particle Driven Geodesic Acoustic Mode

4.1 Introduction to Energetic Particle Driven Geodesic Acoustic Mode

Geodesic acoustic mode (GAM) is an oscillatory zonal flow coupled with density and pressure perturbations in toroidal plasmas[6][7][8]. Geodesic acoustic modes are driven by micro turbulence [9] and can be driven also by toroidal Alfvén eigenmodes[10]. Recently, energetic particle driven geodesic acoustic modes (EGAM) are observed in JET[11], DIII-D[12], and LHD[16][15]. It has been revealed by theoretical and numerical analyses that EGAM is a global mode with finite spatial width that is determined by energetic particle effects[13]. Theoretical analyses have been made for fast excitation due to the

loss boundary in pitch angle[14], for coupling to the GAM continuum[57], and for second harmonics of EGAM[58]. Since the toroidal mode number of GAM is $n = 0$, this mode does not affect toroidal canonical momentum of particle and does not transport particle in radial direction. On the other hand, particle energy evolves during the interaction with GAM. When counter passing particles lose energy, they may become trapped particles whose orbits deviate outward from those of the original passing particles. If the banana orbit width is large enough, the trapped particle may be lost from the plasma. This mechanism might explain the drops in neutron emission observed on DIII-D associated with the EGAM bursts[12].

In this chapter we investigate both the linear properties and the nonlinear evolution of EGAM. The linear properties are fundamental and interesting. The frequency of conventional GAM depends on plasma temperature and safety factor. Then, conventional GAM is localised on magnetic surface. The energetic particle effects give rise to the finite spatial width and make EGAM a global mode. It is interesting to investigate how the EGAM spatial profile depends on the energetic particle distribution and on the safety factor profile. In the experiments, magnetic fluctuations are observed associated with the EGAM. The magnetic perturbations of conventional GAM was theoretically investigated and the poloidal mode number was predicted to be $m = 2$[59]. However, the magnetic perturbations of EGAM has not been investigated yet. It is worth clarifying the EGAM magnetic perturbations. The nonlinear properties are more interesting, and the most exciting phenomenon is frequency chirping. The frequency chirping including both chirping up and chirping down is observed in the experiments. In this thesis, we reproduce the nonlinear frequency chirping and investigate the phase space structure of energetic particles.

This chapter is organized as follows. In section 4.2, the distribution func-

tion and simulation parameters are described. In section 4.3.1, the EGAM linear properties which include the frequency, growth rate, mode number and mode spatial width are examined. Different simulation conditions, for example, different energetic particle β value, different energetic particle spatial width, and different safety factor q profiles, are applied to investigate the linear properties. In section 4.3.2, the nonlinear frequency chirping is reproduced in the simulation result. The energetic particle distribution function is investigated in velocity space. It is found that hole-clump pairs are created and their transit frequencies are in good agreement with the EGAM frequency. In addition, some particles are traced to confirm the relation between mode frequency and particle transit frequency. Numerical convergence in number of computational particles, grid size and time step width is also examined. The section 4.4 is devoted to summary for the simulation results of EGAM.

4.2   Simulation model and parameters

The simulation model is based on that described in chapter 2. For the study of EGAM, the energetic particle beta profile, the ratio of the energetic particle pressure and the magnetic pressure, is assumed to be

$$\beta_h(\psi) = \beta_{h0} e^{-\tilde{\psi}/\xi^2}, \tag{4.1}$$

where $\tilde{\psi}$ is the normalized poloidal flux with $\tilde{\psi} = 0$ at the plasma center and $\tilde{\psi} = 1$ at the plasma edge, β_{h0} is the energetic particle beta value at the magnetic axis. The parameter ξ is a normalized spatial scale length and normally set to be 0.5. But in some cases, this value will be changed to 0.3 or 0.7 to investigate the EGAM linear properties. The β_h profiles are shown in Fig. 4.1, and the effects of β_h profile are discussed in section 4.3.1.
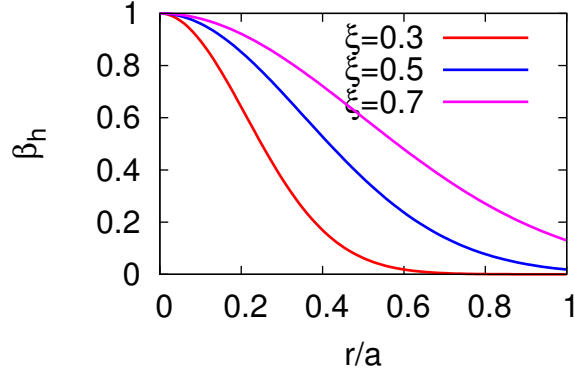
Figure 4.1: Energetic particle beta profiles with different spatial widths. The widths are controlled by parameter ξ in Eq. (4.1). These 3 curves (red, blue and pink) represent $\xi = 0.3$, 0.5 and 0.7, respectively. In the present work, the $\xi = 0.5$ is used mostly.

The equilibrium energetic particle distribution f_0 can be written using constants of motion as

$$f_0 = f_0(E, \mu, P_\phi, \sigma), \tag{4.2}$$

where E is the particle energy, μ is the magnetic moment, P_ϕ is the canonical toroidal momentum. P_ϕ is defined by

$$P_\phi = Z_h e \psi + R m v_\parallel \frac{B_\phi}{B}, \tag{4.3}$$

where $Z_h e$ and m are the particle charge and mass, and ψ is poloidal magnetic flux.

Assuming the separation of variables, Eq. (4.2) is expressed by

$$f_0 = f_0(E, \mu, P_\phi, \sigma) = \mathcal{G}(E)\mathcal{H}(\Lambda)\mathcal{I}(P_\phi, E, \mu, \sigma), \tag{4.4}$$

where $\Lambda = \mu B_0/E$ is pitch angle with B_0 magnetic field strength at the magnetic axis, and σ distinguishes orbit types with $\sigma = 1$ for co-passing particles, 0 for trapped particles, and -1 for counter-passing particles. The

energy distribution $\mathcal{G}(E)$ is a slowing down distribution. The function $\mathcal{H}(\Lambda)$ is introduced to model anisotropic distributions in pitch angle,

$$\mathcal{H}(\Lambda) = exp[-(\frac{\Lambda - \Lambda_{peak}}{\Delta\Lambda})^2], \tag{4.5}$$

where Λ_{peak} represents the pitch angle value for the distribution peak and $\Delta\Lambda$ is a parameter to control the distribution width. The function $\mathcal{I}$ represents the radial profile. To be consistent with the beta profile in Eq. (4.1), $\mathcal{I}$ is given by

$$\mathcal{I}(E, \mu, P_\phi, \sigma) = exp\left(-\psi_{nrm}/\xi^2\right), \tag{4.6}$$

$$\psi_{nrm} = 1 - \frac{P_\phi - \sigma R_0 m v_0}{Z_h e \psi_{max}}, \tag{4.7}$$

$$v_0 = \sqrt{2(E - \mu B_{min})/m}, \tag{4.8}$$

The time derivative of $\delta f = f - f_0$ at each marker particle is

$$\begin{aligned}
\frac{d}{dt}\delta f &= \frac{d}{dt}(f - f_0) = -\frac{d}{dt}f_0 \\
&= -\frac{dE}{dt}\frac{\partial f_0}{\partial E} - \frac{dP_\phi}{dt}\frac{\partial f_0}{\partial P_\phi}.
\end{aligned} \tag{4.9}$$

The time derivative of magnetic moment μ does not appear because it is an adiabatic invariant. In Eq. (4.3), P_ϕ is defined using the equilibrium poloidal flux and is not related to the toroidal vector potential fluctuation of EGAM. Then, P_ϕ evolves slightly in the simulations presented here, whereas EGAM does not affect the toroidal canonical momentum defined with vector potential fluctuation. However, the most important contribution to the EGAM destabilization arises from the energy evolution of the resonant particles,

$$\frac{\partial f_0}{\partial E} = \frac{\partial\mathcal{G}}{\partial E}\mathcal{H}\mathcal{I} + \mathcal{G}\frac{\partial\Lambda}{\partial E}\frac{\partial\mathcal{H}}{\partial\Lambda}\mathcal{I} + \mathcal{G}\mathcal{H}\frac{\partial\mathcal{I}}{\partial E}. \tag{4.10}$$

The destabilization of EGAM arises from the second term, while the first term is stabilizing for the slowing down distribution. Unless otherwise specified, the parameter $\Delta\Lambda$ is set to be 0.2. The $\Delta\Lambda$ value will be modified to 0.1 or
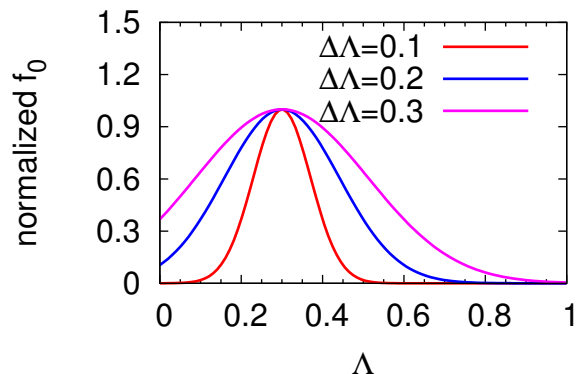
Figure 4.2: Normalized initial energetic particle distribution functions in Λ space described by Eq. (4.5). The parameter $\Delta\Lambda$ is used to control the distribution width. These 3 curves (red, blue and pink) represent 3 different distributions with $\Delta\Lambda = 0.1$, 0.2 and 0.3, respectively. The standard value is $\Delta\Lambda = 0.2$.

0.3 to compare the EGAM frequency and growth rate. The initial energetic particle distribution functions in Λ space are shown in Fig. 4.2, and the simulation results are described in Section 4.3.1.

The cylindrical coordinates (R, ϕ, z) are used, where R is the major radius coordinate, ϕ is the toroidal angle coordinate and z is the vertical coordinate. Since the kinetic GAM frequency in LHD is close to that in tokamaks, tokamak type equilibria are examined with concentric magnetic surfaces, and with the safety factor profiles and the aspect ratio similar to the LHD plasmas. We focus on $n = 0$ modes. The simulation region is $R_0 - a \leq R \leq R_0 + a$, $0 \leq \phi \leq 2\pi$ and $-a \leq z \leq a$, where R_0 is the major radius. The aspect ratio is $R_0/a = 6.0$ with $a = 0.65m$ and $R_0 = 3.9m$. The number of marker particles is 5.24×10^5, but a larger particle number, 2.10×10^6, is also used to investigate the numerical convergence. The viscosity and diffusivity are set to be $\nu = \nu_n = 127.6 m^2/s$ and the resistivity $\eta = 1.603 \times 10^{-4} \Omega \cdot m$ in the simulation.
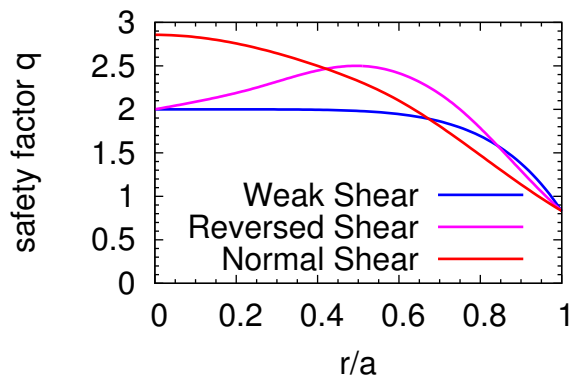
Figure 4.3: Safety factor q profiles. The 3 curves (red, blue and pink) represent normal shear, weak shear and reversed shear case, respectively.

Three different safety factor q profiles, normal type, weak shear type and reversed shear type are investigated. The safety factor profiles are shown in Fig. 4.3. In the case of reversed shear and weak shear q profiles, the number of grid points is 64×16×64 for the cylindrical coordinates (R, ϕ, z), and in the case of normal shear q profile, the number of grid points is 100×16×100.

The simulation parameters are based on an LHD experiment[15], $B_0 = 1.5T$, electron density $n_e = 0.1 \times 10^{19}/m^3$, electron temperature at the magnetic axis $T_e = 4keV$, bulk plasma beta value at the magnetic axis 7.2×10^{-4}. Figure 4.4 shows the density profile and the temperature profiles. In order to investigate the temperature dependence of the EGAM frequency, different temperature profiles are used in present work. The safety factor q profiles are also based on experiments. The normal shear and weak shear q profiles are based on Ref. [15], and the reversed shear q profile is based on Ref. [16].
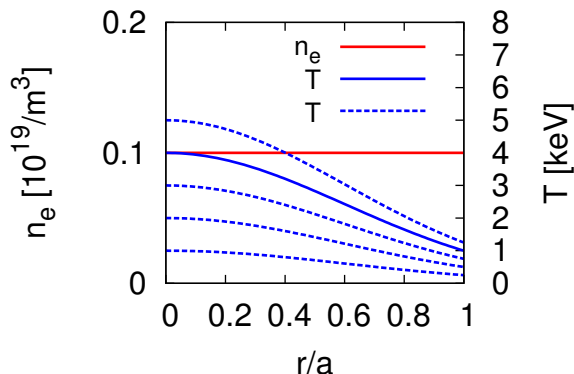
Figure 4.4: Spatial profiles of plasma density and temperature. Red curve represents density, and solid blue curve represents the standard temperature profile. Dashed blue curves are the test temperature profiles for the investigation of temperature dependence of mode frequency.

4.3 Simulation results

4.3.1 Linear properties of energetic particle driven geodesic acoustic mode

4.3.1.1 Spatial profile

The spatial profiles of the EGAM in LHD are shown in Fig. 4.5. The plasma poloidal velocity v_θ on a poloidal cross section is shown in Fig. 4.5(a). We can see the poloidal mode number $m = 0$, and the absolute velocity is higher in the low field side. The variation of velocity on a magnetic surface leads to the lack in density uniformity, and $m = 1$ density perturbation δn_e appears on a poloidal cross section as shown in Fig. 4.5 (b). The poloidal and radial magnetic perturbations B_θ and B_r are shown in Fig. 4.5 (c) and Fig. 4.5 (d). We see the poloidal mode number is $m = 2$. These 4 panels are plotted for the linear phase at same time. All of the above mode numbers are consistent with
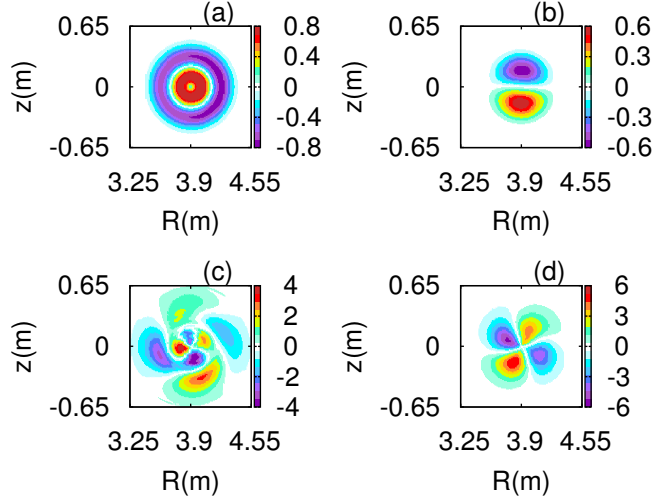
Figure 4.5: EGAM perturbations on a poloidal cross section, (a) poloidal velocity v_θ [km/s], (b) plasma density [%], (c) poloidal magnetic field [10^{-6}T], and (d) radial magnetic field [10^{-6}T]. The dominant poloidal mode numbers are (a) $m = 0$, (b) $m = 1$, (c) $m = 2$, and (d) $m = 2$.

the theoretical predictions[6][59] and the experimental observations[11][12][16][15].

4.3.1.2   Mode destabilization

The normalized equilibrium particle distribution in $\Lambda - E$ space is plotted in Fig. 4.6 to illustrate the EGAM destabilization mechanism. As mentioned above, the initial distribution is a slowing-down distribution in energy, and Gaussian in pitch angle. The dashed curves represent constant μ, and particles move only along the dashed curves because μ is an adiabatic invariant. In area A, $\frac{\partial f}{\partial E}|_{\mu=constant} > 0$, and the particles with positive $\frac{\partial f}{\partial E}$ can destabilize EGAM. In area B, $\frac{\partial f}{\partial E}|_{\mu=constant} < 0$, and particles in this area are not able to excite EGAM.

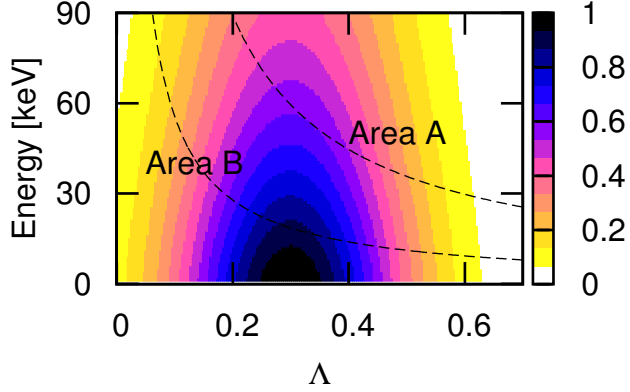The energy transfer rate in the linear phase with $E_{NBI} = 170 keV$ and

Figure 4.6: Normalized initial particle distribution in $\Lambda - E$ space. Dashed curves represent constant μ. Only the particles in area A can destabilize EGAM because $\frac{\partial f}{\partial E}|_{\mu=constant} > 0$. Particles with energy higher than 90keV or pitch angle larger than 0.7 are not shown here.

$\Lambda_{peak} = 0.3$ is plotted in Fig. 4.7. It shows $w\frac{dE}{dt}$ [unit: a.u.] in $\Lambda - E$ space, where w is the particle weight. The dashed curves represent constant μ. The purple color represents negative $w\frac{dE}{dt}$, that means the energy transfers from particles to EGAM, destabilizing the EGAM. In contrast, red color represents positive energy transfer, and the mode is stabilized. The energy transfer rate in the destabilization region is higher than that in the stabilization region. Then, EGAM is excited on the whole. Notice that the purple region in Fig. 4.7 is the same as area A in Fig. 4.6, and the red region in Fig. 4.7 is the same as area B in Fig. 4.6. These 2 figures are consistent with each other to clarify the mode destabilization mechanism.

4.3.1.3 Mode frequency and growth rate

4.3.1.3.1 Global mode The EGAM perturbation frequency and the conventional local GAM frequency are shown as functions of normalized minor radius in Fig. 4.8. From $r/a = 0.05$ to $r/a = 0.95$, 10 points are selected
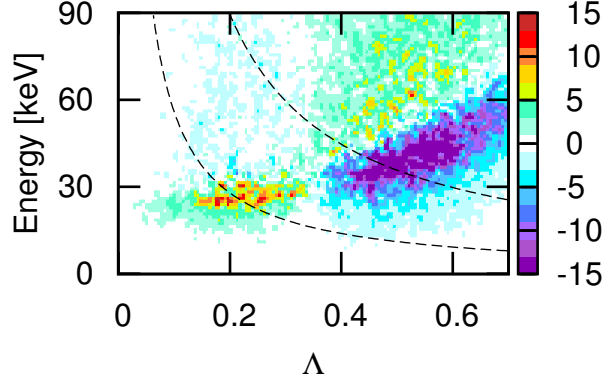
Figure 4.7: Energy transfer rate $w\frac{dE}{dt}$ [unit: a.u.] in $\Lambda - E$ space. Dashed curves represent constant μ. EGAM is destabilized by the particles in the purple region because $\frac{dE}{dt} < 0$.

equidistantly. On these points, the EGAM frequencies are investigated, and the conventional GAM frequencies are calculated by $f = \sqrt{(2\gamma p/\rho R_0^2)(1 + \iota^2/8\pi^2)}/(2\pi)$, $\iota = 1/q$ is the rotational transform. The conventional local GAM frequency constitutes the continuous spectrum that varies depending on the plasma temperature and the safety factor. In the case of LHD, the conventional GAM continuum is higher at the plasma center and lower on the edge. Contrast to the conventional GAM frequency, the EGAM frequency is a horizontal line, and it intersects the conventional GAM continuum. The difference between the maximum and minimum EGAM frequencies is less than 0.5%. This indicates that the EGAM is a global mode whose frequency is spatially constant. The difference between EGAM and conventional GAM has been experimentally clarified in DIII-D[12]. The result presented here is consistent with the experiment.

4.3.1.3.2   Temperature dependence   According to theoretical prediction[6][8][9], the conventional GAM frequency should be proportional to the square root of plasma temperature. For EGAM case, the relation between frequency and
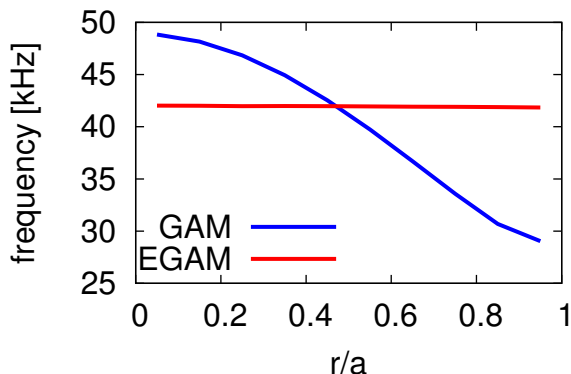
Figure 4.8: Conventional GAM continuum (blue line) and EGAM frequency in the simulation (red line) versus normalized minor radius. The conventional GAM frequency is higher at plasma center and lower on the edge because it depends on temperature and safety factor. By contrast, EGAM is global and its frequency is spatially constant.

temperature is not clear in theory, but observed in experiment[15]. Similar with conventional GAM, the EGAM frequency is proportional to the square root of temperature in LHD. This relation is also observed in the present simulation results, as shown in Fig. 4.9. The red dots represent simulation data, and the blue line is a linear fit to the data. In these cases, $E_{NBI} = 170 keV$, energetic particle pressure $\beta_h = 0.3\%$, $\Lambda_{peak} = 0.3$ and q profile is weak shear. We see clearly the linear relation between mode frequency and $\sqrt{T}$.

4.3.1.3.3 Energetic particle pressure dependence In Ref. [12], the energetic particle pressure dependence of the mode frequency and linear growth rate is investigated with simulation. In the present work, this relation is also investigated and shown in Fig. 4.10. The solid red line represents mode frequency, and the dashed blue line is for the linear growth rate. In these simulations, $E_{NBI} = 170 keV$, $T_e = 4 keV$, $\Lambda_{peak} = 0.3$ and q profile is weak shear. We see the mode frequency decreases and linear growth rate
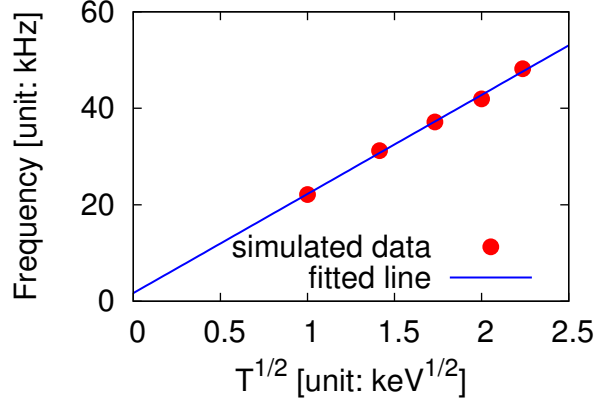
Figure 4.9: Relation between EGAM frequency and square root of plasma temperature. Red dots represent simulation data, and the blue line is a linear fit to the data. The mode frequency is proportional to $\sqrt{T}$.

increases with β_h increases.

In order to compare with the pure MHD model[6], the energetic particles are turned off and the frequency is analysed. Near the plasma center, the frequency without energetic particle is $45.2kHz$, and the theoretically predicted frequency in MHD framework should be $47.7kHz$. These frequencies are quite closed to each other.

4.3.1.3.4 Energetic particle distribution width dependence The mode frequency and growth rate are also affected by energetic particle spatial distribution width. The various spatial distributions are shown in Fig. 4.1. The frequencies and growth rates with these 3 distributions are plotted in Fig. 4.11. The figure indicates that the frequency and growth rate decrease as ξ increases.

Not only energetic particle spatial distribution width but also pitch angle distribution width change the mode frequency and growth rate. The dif-

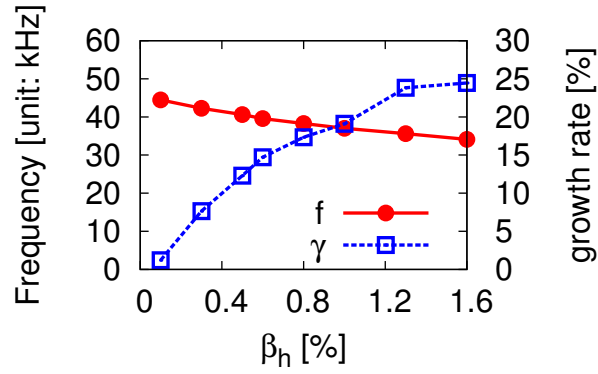Figure 4.10: Energetic particle pressure dependence of the mode frequency (red) and linear growth rate (blue). The mode frequency decreases and the linear growth rate increases as β_h increases.
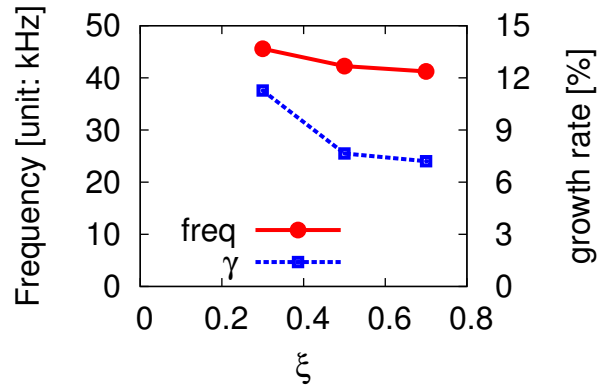

Figure 4.11: Energetic particle spatial distribution width dependence of the mode frequency (red) and linear growth rate (blue). The mode frequency and linear growth rate decrease as distribution width ξ increases.
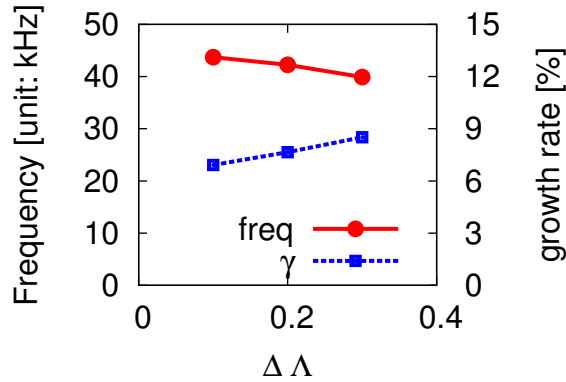
Figure 4.12: Energetic particle pitch angle distribution width dependence of mode frequency (red) and linear growth rate (blue). The mode frequency decreases and the linear growth rate increases as $\Delta\Lambda$ increases.

ferent pitch angle distributions are shown in Fig. 4.2, while the frequency and growth rate with these 3 conditions are represented in Fig. 4.12. We see in this figure that the mode frequency decreases and linear growth rate increases as $\Delta\Lambda$ increases.

4.3.1.4 Mode spatial width and propagation

4.3.1.4.1 Mode spatial width and q profiles The mode spatial width in the linearly growing phase is investigated for different q profiles plotted in Fig. 4.3. In the case of normal shear q, the mode spatial width is not wide as shown in Fig. 4.13 (a). The color bar shows the mode amplitude v_θ, and the unit is km/s. The horizontal axis is the normalized minor radius, and the mode width is related with the width of color area. In the case of weak shear q, the mode spatial width broadens as shown in Fig. 4.13 (b). In the case of reversed shear q, the mode spatial width is broadened more as shown in Fig. 4.13 (c). In these cases, the other simulation parameters are the same, $T_e = 4$ keV, $E_{NBI} = 170$ keV, $\Lambda_{peak} = 0.3$, $\beta_h = 0.3\%$, and energetic particle

spatial width $\xi = 0.5$. The data before $t = 0.23$ ms and after $t = 0.27$ ms is not shown but the results are similar in the linear phase. We can see the mode propagation in these figures. In Fig. 4.13 (c), the bottom value of mode amplitude departures around $r/a = 0$ at $t = 0.235$ ms, and reaches $r/a = 0.8$ at $t = 0.265$ ms. It propagates outward, and takes longer time than case (a) and case (b). This indicates that the reversed shear broadens the mode spatial width and also reduces the mode propagation speed.

4.3.1.4.2 Mode spatial width and distribution width ξ The mode spatial width is affected not only by q profile but also by energetic particle spatial width ξ. In Fig. 4.1, 3 different energetic particle spatial distributions with various widths have already been shown. Simulation under these 3 situations are carried out to clarify the relation between mode spatial width and distribution width ξ. In the case of $\xi = 0.3$, the mode spatial width is not very wide as shown in Fig. 4.14 (a). For $\xi = 0.5$ case, the mode spatial width is broader as shown in Fig. 4.14 (b). In the $\xi = 0.7$ situation, the mode spatial width becomes wider as shown in Fig. 4.14 (c). We can conclude that the wider energetic particle spatial width leads to wider mode spatial width. For these 3 cases, the other simulation parameters are the same, $T_e = 4$ keV, $E_{NBI} = 170$ keV, $\Lambda_{peak} = 0.3$, $\beta_h = 0.3\%$, and q profile is weak shear. In addition, wider energetic particle spatial width causes lower propagation speed. Considering Fig. 4.13 and Fig. 4.14 together, we know the wider mode spatial width is related with lower propagation speed.
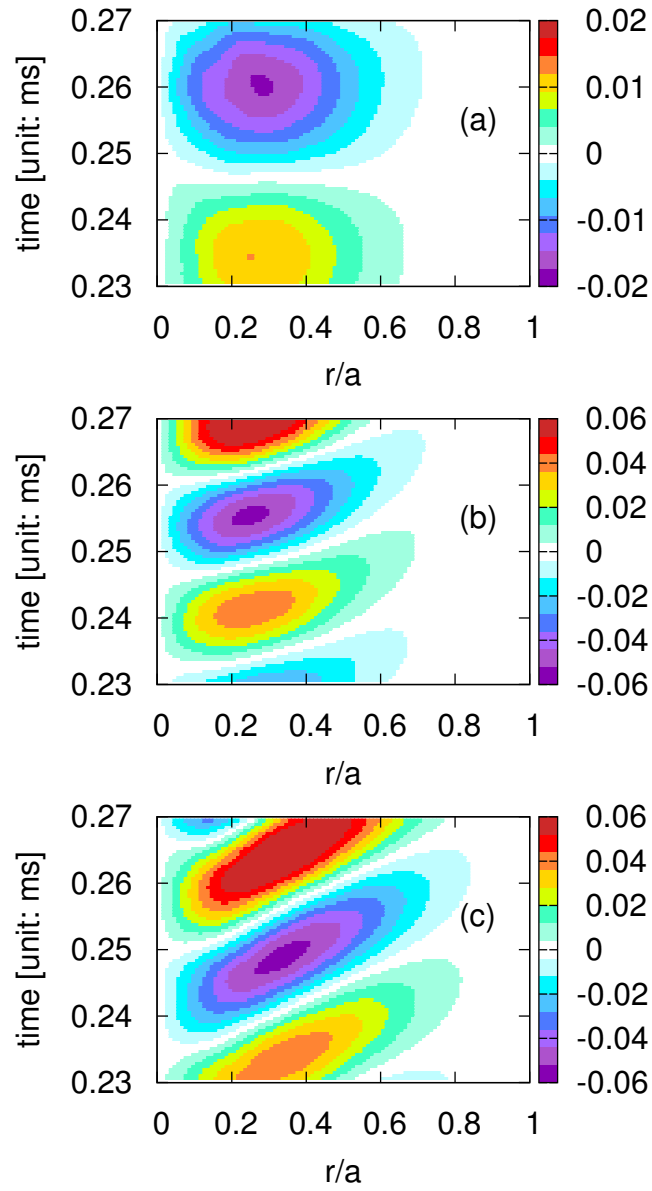
Figure 4.13: Time evolution of poloidal velocity profile for (a) normal q profile, (b) weak shear q profile, and (c) reversed shear q profile. The unit of color bar is km/s.
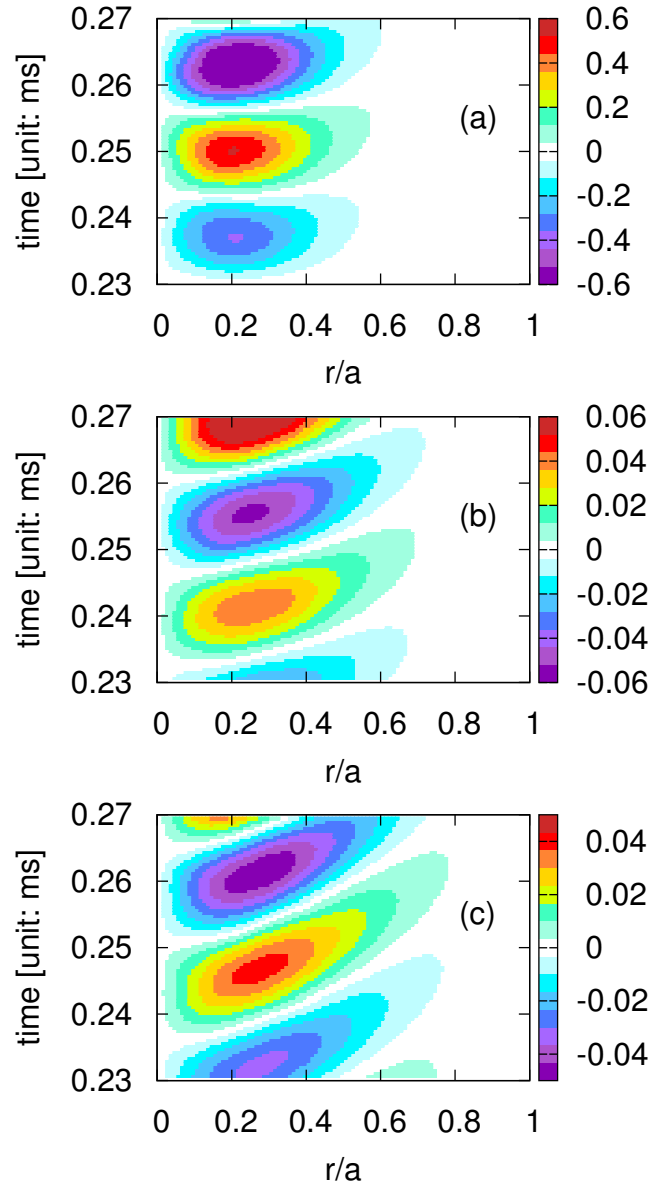
Figure 4.14: Time evolution of poloidal velocity profile for (a) energetic particle spatial width $\xi = 0.3$, (b) $\xi = 0.5$, and (c) $\xi = 0.7$. The unit of color bar is km/s.
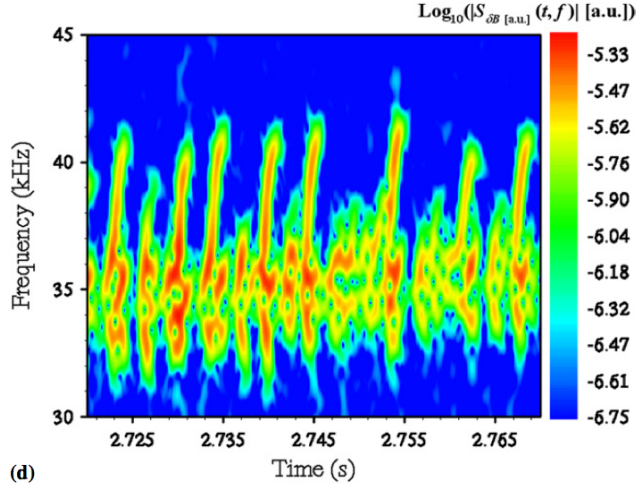
Figure 4.15: Frequency evolution of $n = 0$ mode in JET. The mode frequency chirps up and down.

4.3.2 Nonlinear properties of energetic particle driven geodesic acoustic mode

4.3.2.1 Frequency chirping

EGAM is observed in JET[11] as shown in Fig. 4.15. The frequency chirps up rapidly from 35kHz to 40kHz in 2ms. In addition, another branch chirps down, but the chirping down branch is weaker than the chirping up one. Similar results are also observed in LHD[15] as shown in Fig. 4.16. The mode frequency chirps up from 30kHz to 80kHz in 10ms. It is impossible for conventional GAM to chirp so rapidly.

The EGAM frequency chirping takes place in a simulation run with weak shear q profile with $\Lambda_{peak} = 0.3$. The frequency evolution is shown in Fig. 4.17. The mode frequency chirps up from 40kHz to 50kHz in 0.4ms. Another branch chirps down, but this branch is weaker than the chirping up branch. This feature is similar with the experimental results in JET shown

55

Figure 4.16: Frequency evolution in LHD. The toroidal mode numbers were measured using toroidal magnetic probe array in LHD. EGAM is marked in black color. The mode frequency chirps up rapidly.

in Fig. 4.15.

4.3.2.2 Hole and clump pairs in (Λ, E) space

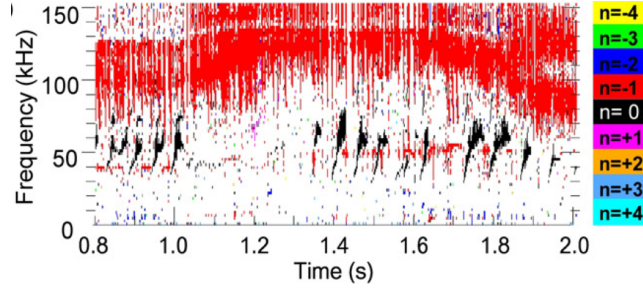The EGAM frequency chirping is fascinating, and the mechanism needs to be explained. The Berk-Breizman model has successfully explained frequency sweeping modes, e.g. Alfvén eigenmode and ICRF driven EGAM.[60][61][11] This model reveals spontaneous formation of coherent phase space structures (hole and clump) with frequency chirping. We compare the simulation results with the Berk-Breizman model.

The energetic particle δf distribution in two-dimensional velocity space (Λ, E) is shown in Fig. 4.18 for $t = 0.55$ ms, $t = 0.80$ ms and $t = 1.25$ ms. The blue color represents $\delta f < 0$ (hole) while the red for $\delta f > 0$ (clump). The δf distribution is integrated over the whole simulation domain. The dashed curves represent constant magnetic moment $(\mu = \Lambda E / B_0)$ that is an adiabatic invariant. We see in the figure that two pairs of hole and clump are created along the constant μ curves in (Λ, E) space. One pair is created along the higher-μ curve with a hole in the high energy side and a clump in the low energy side. Note that this pair is created in the region destabilizing the

56
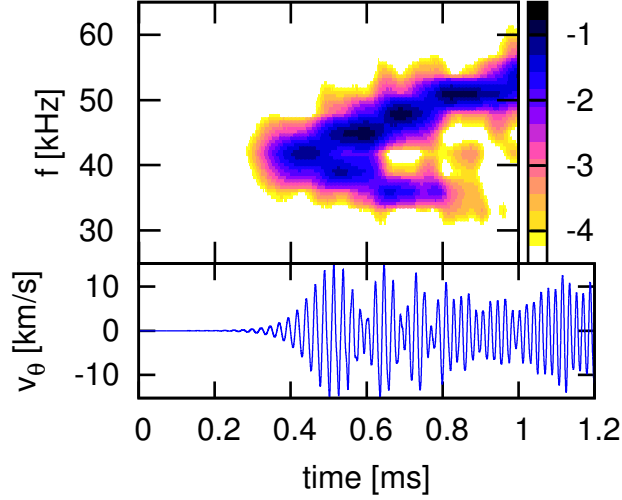
Figure 4.17: Time evolution of EGAM poloidal velocity v_θ (bottom) and the power spectrum (top). The horizontal axis is shared by both the panels. Color bar indicates the magnitude in logarithmic scale.

instability denoted as Area A in Fig. 4.6. This pair is consistent with Berk-Breizman model where a hole (clump) is created in the high (low) energy side. The other pair is created along the lower-μ curve in the stabilizing region Area B in Fig. 4.6. We see a clump in the high energy side and a hole in the low energy side. This is the first discovery of the creation of hole-clump pair in the stabilizing region in phase space.

Solid curves in Fig. 4.18 represent the constant poloidal transit frequency defined by

$$f_{tr} = \sqrt{1 - \Lambda} v / (2\pi q R_0), \tag{4.11}$$

where v is particle velocity and q is the safety factor value. The energetic particle beta profile shown in Fig. 4.1 and the EGAM spatial profile shown in Fig. 4.13 indicate that the interaction between the energetic particles and the EGAM takes place in the region $r/a \leq 0.6$. Then, we set $q = 2$ for f_{tr} because this is a good approximation for $r/a \leq 0.6$ with the weak shear q

Figure 4.18: Energetic particle δf distribution in (Λ, E) space at (a) $t = 0.55$ ms, (b) $t = 0.80$ ms and (c) $t = 1.25$ ms. Solid curves represent constant f_{tr}, and dashed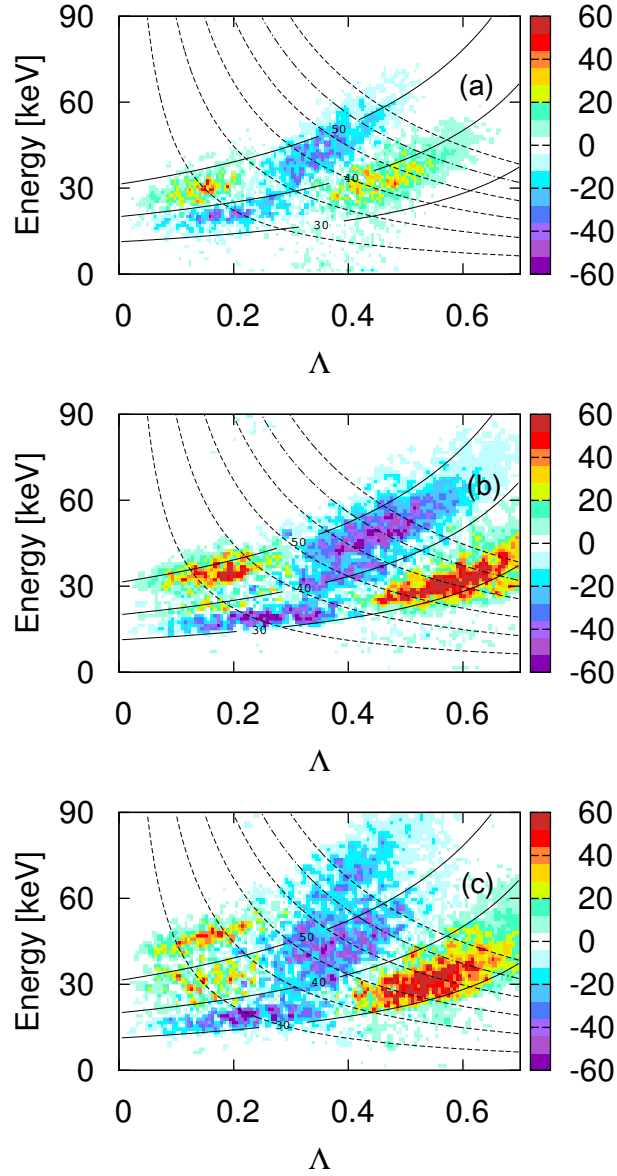 curves represent constant μ (the dot-dashed curve represent $\mu = 15$ keV/T curve). Two hole-clump pairs are created.

profile shown with blue curve in Fig. 4.3. The resonance condition between energetic particle and EGAM is given by $f = f_{tr}$. If the transit frequency is in agreement with the EGAM frequency, the particle is resonant with the EGAM.

In time evolution, it is possible for particles to move across solid curves. At $t = 0.55$ ms, as shown in Fig. 4.18(a), the transit frequency of the left clump (or the clump with lower μ value) is about 45 kHz. At $t = 0.80$ ms as shown in Fig. 4.18(b), the clump shifts upward along the dashed curve, and transit frequency becomes 49 kHz. At $t = 1.25$ ms as shown in Fig. 4.18(c), the transit frequency of that clump exceeds 55 kHz. Similarly, the right hole (or the hole with higher μ value) is also shifting upward along the dashed curve, and the transit frequency increases. On the other hand, the left hole and right clump (or the hole with lower μ and the clump with higher μ) shift downward in time evolution, and the transit frequencies decreases. The transit frequencies of right hole and left clump are increasing, and they correspond to the chirping up branch in Fig. 4.17. The left hole and right clump correspond to the chirping down branch. This indicates the particles in the holes and clumps are kept resonant with the EGAM.

4.3.2.3 Time evolution of transit frequency

For more accurate comparison of the transit frequency with the EGAM frequency, the distribution perturbation δf is plotted versus transit frequency for different times along the $\mu = 15$ keV/T curve (the dot-dashed curve in Fig. 4.18) in Fig. 4.19. The particles with μ value between 14.25 keV/T to 15.75 keV/T are analyzed. The peaks on the left in the figure correspond to the clump, and valleys on the right corresponds to the hole. The frequencies of the maximum and minimum δf are marked with straight lines. At $t = 0.51 ms$, the transit frequency of the bottom is $43 kHz$. In time evolution,
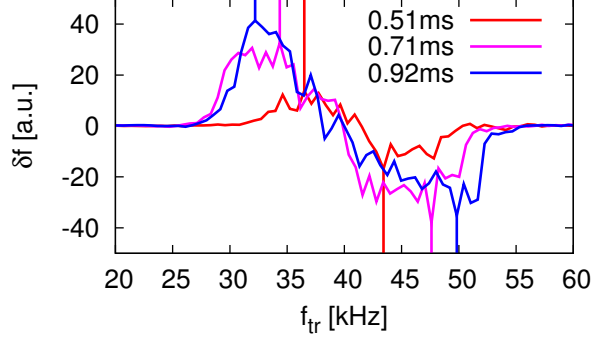
Figure 4.19: Distribution perturbations δf along the $\mu = 15$ keV/T curve (the dot-dashed curve in Fig. 4.18) versus particle transit frequency f_{tr} for different times. The frequency of the maximum and minimum δf is marked with straight lines.

the bottom shifts to the higher transit frequency. At $t = 0.92ms$, the transit frequency reaches to $50kHz$. This is a distinct process of transit frequency rising. It is also clear to illustate the process of clump frequency chirping down.

In order to compare the transit frequency of the hole and the EGAM frequency, the data in Fig. 4.19 is mapped into Fig. 4.17, and the new figure is shown in Fig. 4.20. As well as Fig. 4.17, Fig. 4.20 shows the time evolution of mode power spectrum with colorful dots (and square). The green dots represent the transit frequencies of the hole, and the cyan squares represent the transit frequencies of the clump. We see that the transit frequency of the hole and clump is in good agreement with the EGAM frequency. This indicates the EGAM frequency and the transit frequency of the hole (or clump) increase (or decrease) synchronously.

Figure 4.20: Time evolution of EGAM poloidal velocity v_θ (bottom) and the power spectrum (top). The horizontal axis is shared by both the panels. Color bar indicates the magnitude in logarithmic scale. Green dots represent transit frequencies of hole, and cyan squares represent transit frequencies of clump. They are plotted along $\mu = 15$ keV/T curve.

4.3.2.4 Transit frequency of traced particles

In order to fully investigate the relation between mode frequency of EGAM and the transit frequency of hole-clump pairs, we trace particles in the hole and clump regions. At $t = t_{begin}$, one particle in a hole (or a clump) is marked, and the transit frequency is recorded. Next, this particle is traced, and the transit frequency at $t = t_1, t_2, t_3, ..., t_{end}$ is calculated. Then, the track of this particle can be plotted in frequency-time coordinate. Apply this method to more particles, and map their tracks into Fig. 4.17, then a new figure can be obtained as shown in Fig. 4.21. As well as Fig. 4.17, figure 4.21 is also time evolution of mode power spectrum, but some more curves are added. In Fig. 4.18, the μ value of left hole and left clump is small, and the tracks of particles with lower μ are plotted in Fig. 4.21 (a). For lower μ case, 20 particles are tracked. In Fig. 4.21 (b), other 20 particles with higher μ are tracked. The black curves represent the tracks of particles in the holes, and the green tracks represent those in the clumps. The transit frequencies of particles in lower μ clump and higher μ hole chirp up, whereas they chirp down for particles in lower μ hole and higher μ clump. The transit frequencies of these particles are consistent with mode frequency. This clearly demonstrates that the particles in the holes and clumps are kept resonant with the EGAM.

4.3.3 Convergence studies

In order to confirm the simulation results, numerical convergences have been investigated with regard to the number of particles and the number of grids on poloidal cross section. Different particle numbers and grid numbers are tested, and the time evolutions of mode amplitude are similar with each other, as shown in Fig. 4.22. In the case of less particle and grid number, the mode
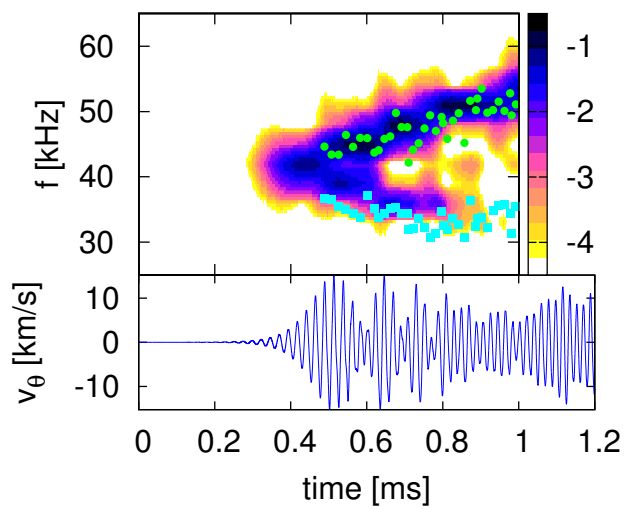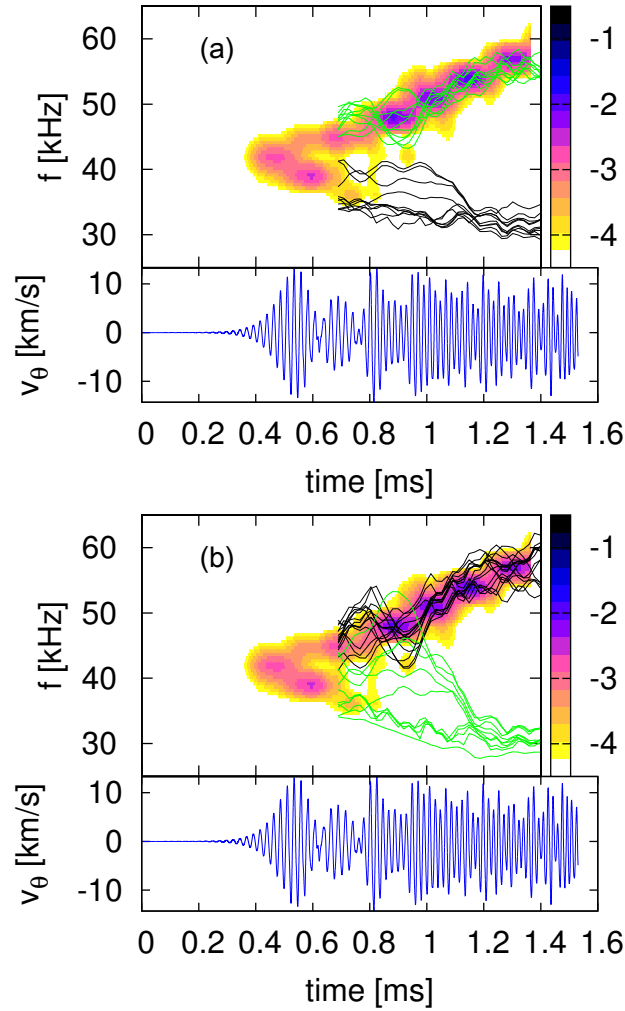
Figure 4.21: Time evolution of EGAM poloidal velocity v_θ (bottom) and the power spectrum (top). The horizontal axis is shared by both the panels. Color bar indicates the magnitude in logarithmic scale. The black curves represent the transit frequency evolution of particles in the holes, and the green curves represent that in the clumps for (a) low μ and (b) high μ.
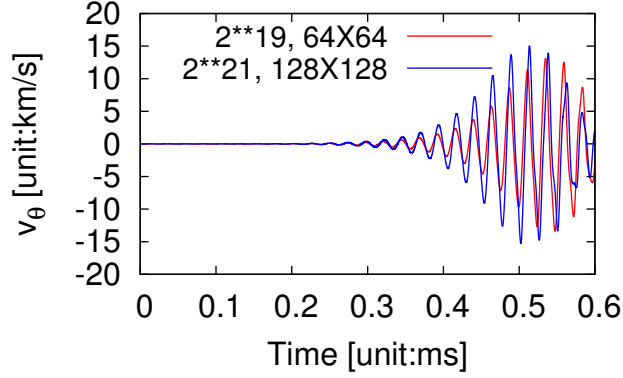
Figure 4.22: Time evolution of the poloidal velocity for different numbers of particles and grids. The total number of particles used in the blue curve is 2^{21}, 4 times larger than that used in the red one. The total grid number on poloidal cross section is 128 in r direction and 128 in z direction (16384 grids in total), also 4 times larger than that in another case. Other simulation conditions are the same in these 2 cases.

linear growth rate and frequency are 7.7% and 42.3kHz, respectively; whereas for more particle and grid number case, growth rate is 8.2% and frequency is 42.0kHz. The growth rate and the saturation level are independent of the particle number and the grid number in these simulations. In addition, less grid number means bigger grid size, and step width in this case is also larger, so the result is independent of the step width as well. As a conclusion, the numerical convergence is good enough for the results presented in this thesis.

4.4   Summary

EGAM is an important issue in current fusion science and technology. In this thesis, EGAM linear properties which include the frequency, growth rate, mode number and mode spatial width are investigated using a hybrid

simulation code for MHD and energetic particles, MEGA. In addition, with the same code, the mechanism of nonlinear EGAM frequency chirping is clarified in different ways. The behaviours of EGAM under various simulation conditions have been compared carefully.

4.4.1   Linear properties

It is found that the EGAM is a global mode because the fluctuation frequency is spatially constant, whereas the conventional local GAM frequency constitutes the continuous spectrum that varies depending on the plasma temperature and the safety factor. The frequency of the EGAM intersects with the GAM continuous spectrum.

Similar with conventional GAM frequency, the EGAM frequency is also found to be proportional to the square root of the plasma temperature. This is consistent with experimental observation, and it is the first attempt to investigate such relation for EGAM by means of simulation. In addition, it is found that the simulated EGAM frequency is lower and linear growth rate is higher for higher β_h, this tendency is the same as G. Y. Fu's theory and simulation[13, 12]. The energetic particle distribution width dependence of the mode frequency and growth rate is also investigated. As spatial width increases, both the mode frequency and the mode growth rate decrease; while as pitch angle width increases, mode frequency decreases but growth rate increases.

Mode spatial profile is another interesting topic. It is found that the mode spatial width are different for various q profiles. In the case of normal q profile, the mode spatial width is not very wide. In the case of weak shear q profile, mode spatial width is broader. For reversed shear q profile, mode spatial width is the widest. The relation between mode spatial width and

energetic particle spatial width is also investigated. Larger energetic particle spatial width can cause larger mode spatial width. It is also found that the mode propagation speed is related with the mode spatial width.

According to the simulation results, the poloidal mode number of plasma poloidal velocity, plasma density perturbation and magnetic field strength perturbation are $m = 0$, $m = 1$ and $m = 2$, respectively. It is consistent with both theoretical prediction and experimental observation. And finally, theoretically speaking, EGAM is destabilized by the particles with positive $\partial f/\partial E$, and this viewpoint is confirmed by the energy transfer analysis.

4.4.2   Nonlinear frequency chirping

EGAM frequency chirping is found in LHD and tokamaks. In the present simulation, both the mode frequency upward chirping and downward chirping take place, and the downward branch is weaker than the upward one. It is consistent with the experimental observation.

In order to clarify the mechanism of EGAM frequency chirping, the energetic particle δf distribution is analyzed in (Λ, E) space. The advantage of plotting δf in (Λ, E) space is that both the magnetic moment μ and particle transit frequency f_{tr} can be shown clearly. The analysis revealed that two pairs of hole and clump are created, one in the destabilizing region and the other in the stabilizing region in (Λ, E) space. It is found that the transit frequency of particles in low μ clump and high μ hole shifts up in time evolution, whereas it shifts down for particles in low μ hole and high μ clump. In addition, δf distribution with the high μ value are investigated as a function of poloidal transit frequency. The transit frequency of the hole rises synchronously with the EGAM frequency chirping up. This confirms the particles in the hole are kept resonant with the EGAM. Furthermore, the

time evolution of transit frequencies of 40 particles in the holes and clumps is investigated and compared with the EGAM frequency. The transit frequency of particles in low μ clump and high μ hole chirps up synchronously with mode frequency chirping up, whereas the particle f_{tr} in low μ hole and high μ clump chirps down with that of the chirping down branch. The transit frequencies of holes and clumps are in good agreement with the mode frequencies. This demonstrates that the particles in the holes and clumps are kept resonant with the EGAM.

This is the first numerical demonstration of frequency chirping and hole-clump pair creation for EGAM, and the first time to investigate the hole-clump pairs in 2-dimensional velocity space (Λ, E). What should be emphasized is that one hole-clump pair is created in the stabilizing region in phase space. Then, the clump propagates towards high energy and the hole towards low energy. The hole and clump in the stabilizing region continue to absorb energy from the EGAM during the frequency chirping. This is an interesting and important discovery that indicates once the hole-clump pairs are created, energy is continuously transferred from the destabilizing phase space region (or destabilizing particle species) to the stabilizing region (species) through the resonant interaction with the wave.

Chapter 5

Summary and future work

5.1 Summary

Energetic particle driven instabilities are important issues for fusion plasmas because they lead to energetic particle transport and losses. Especially for fusion burning plasmas, where the energetic alpha particles play the leading role in the fuel plasma heating, the energetic particle driven instabilities should be suppressed or mitigated for the better confinement of the energetic alpha particles. Then, the understanding of the fundamental properties of energetic particle driven instabilities will contribute to the successful operation of the future fusion reactors. In this dissertation, the linear properties and the nonlinear evolution of energetic particle driven Alfvén eigenmodes and geodesic acoustic modes (GAM) are investigated using a hybrid simulation code for magnetohydrodynamics (MHD) and energetic particles.

The interaction between energetic particles and Alfvén eigenmodes in reversed shear tokamak plasmas are investigated for different minimum safety-factor values. When the energetic particle distribution is isotropic in velocity space, it is demonstrated that the transition from low-frequency reversed s-

hear Alfvén eigenmode (RSAE mode) to toroidal Alfvén eigenmode (TAE mode) takes place as the minimum safety-factor value decreases. The frequency rises up from a level above the GAM frequency to the TAE frequency. It is found that the energetic particles both co- and counter-going to the plasma current are transported by the TAE mode, whereas the co-going particles are primarily transported by the low-frequency RSAE mode. When only the co-passing particles are retained, the low-frequency RSAE modes are primarily destabilized. On the other hand, the high-frequency RSAE modes are destabilized when only the counter-passing particles are retained.

The linear properties and the nonlinear evolution of energetic particle driven GAM (EGAM) are explored for the Large Helical Device (LHD) plasmas. Since the kinetic GAM frequency in LHD is close to that in tokamaks, tokamak type equilibria are examined with concentric magnetic surfaces, and with the safety factor profiles and the aspect ratio similar to the LHD plasmas. For the linear properties, it is found that the EGAM is a global mode because the fluctuation frequency is spatially constant, whereas the conventional local GAM frequency constitutes a continuous spectrum that varies depending on the plasma temperature and the safety-factor. The frequency of the EGAM intersects with the GAM continuous spectrum. The EGAM frequency is lower for the higher energetic particle pressure. The poloidal mode numbers of poloidal velocity fluctuation, plasma density fluctuation, and magnetic fluctuation are $m = 0$, 1, and 2, respectively. Good agreement is found between the LHD experiment and the simulation result in the EGAM frequency and the mode numbers. The EGAM spatial profile depends on the energetic particle spatial distribution and the equilibrium magnetic shear. The wider energetic particle spatial profile broadens the EGAM spatial profile. The EGAM spatial profile is wider for the reversed magnetic shear than for the normal shear.

The nonlinear evolution of EGAM is studied using the hybrid simulation code. The frequency chirping of EGAM has been observed in LHD and tokamaks. The frequency chirping up and down is found to take place in the simulation results. In order to understand the physics mechanism of the frequency chirping, the energetic particle distribution function and the energy transfer rate from the particles to the wave are analyzed in 2-dimensional velocity space of energy and pitch angle variable. In the linearly growing phase of the instability, two resonant regions, one destabilizing and the other stabilizing the EGAM, are found in the velocity space. In the nonlinearly frequency chirping phase, a pair of hole and clump is created at each resonant region. A hole and a clump correspond to negative and positive fluctuation, respectively in the distribution function. Then, two pairs of hole and clump are created, one at the destabilizing region and the other at the stabilizing region. The transit frequencies of the holes and clumps are compared with the EGAM frequency. The transit frequencies of the holes and clumps are in good agreement with the two branches of the EGAM frequency, one chirping up and the other chirping down. This indicates that the holes and clumps are kept resonant with the EGAM and the frequency chirping can be attributed to the hole-clump pair creation. The hole-clump pair creation and the associated frequency chirping are known to take place when the system is close to the instability threshold for the inverse Landau damping. However, the direct numerical simulations have so far been limited to the hole-clump pair creation at the destabilizing region in 1-dimensional velocity space. The result presented in this dissertation is the first numerical demonstration of a) hole-clump pair creation and frequency chirping for EGAM, b) two pairs creation at the destabilizing and the stabilizing regions, and c) hole-clump pairs in 2-dimensional velocity space.

5.2 Future work

The following four investigations are left for our future work. Firstly, we plan to examine EGAM in a systematic way the difference in stability between co- and counter-injection. In LHD, the power of co- and counter-NBIs are balanced[15]. But in DIII-D, the EGAM is obtained under the counter-injection condition[12]. It is interesting to compare them. Secondly, the hole and clump structures of EGAM are only shown by the perturbation of distribution (δf), but it is not enough. It is better to plot the total distribution, that means $f_0 + \delta f$. The total distribution can make the results stronger. Thirdly, the EGAM amplitude oscillation takes place in the nonlinear phase as shown in Fig. 4.17. A preliminary investigation suggests a correlation between the amplitude oscillation and the sign of the energy transfer from the energetic particles. However, the quantitative relationship between them has not been revealed clearly, and it is worth investigation. Lastly, the change of EGAM propagation direction in the nonlinear phase is found in the simulation results. The mode propagates outward in the linear phase, but it moves inward after saturation, and sometimes outward again. The mechanism of this phenomenon needs to be understood.

As an extension of the present EGAM simulation study, more runs should be carried out with different energetic particle distribution functions. In both LHD[15] and DIII-D[12], the EGAM is excited in a short time after the NBI injection. The excitation time is $\sim 0.6s$ and $\sim 0.12s$ in LHD and DIII-D, respectively. It is much shorter than the energetic particle slowing-down time ($\sim 10s$ and $\sim 0.3s$). More interesting phenomena might be discovered with more realistic energetic particle distribution functions.

Appendix A

Alfvén continuum gaps for TAE and RSAE

Alfvén continuous spectrum (continuum) gives us an insight to understand the properties of Alfvén eigenmodes. Alfvén continuum is illustrated and the continuum gaps are compared for TAE and RSAE.

A.1   Alfvén continuum

Before TAE and RSAE are found, the global Alfvén eigenmode (GAE) was investigated for cylindrical geometry[62]. Figure A.1[63] shows the most simple Alfvén continua. The continuum of different poloidal mode number does not intersect with each other. The continuum frequency is given by

$$\omega = \left| \frac{v_A}{R}(n - \frac{m}{q}) \right|, \tag{A.1}$$

where v_A is the Alfvén velocity and q is the safety factor. Generally, continua with different poloidal mode numbers intersect with each other as shown in Fig. A.2[64].
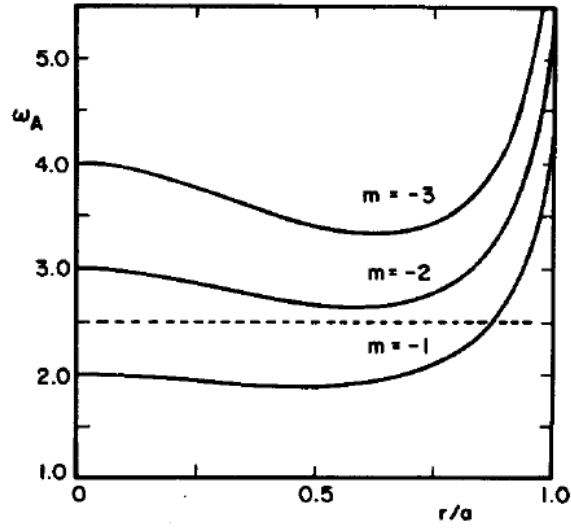
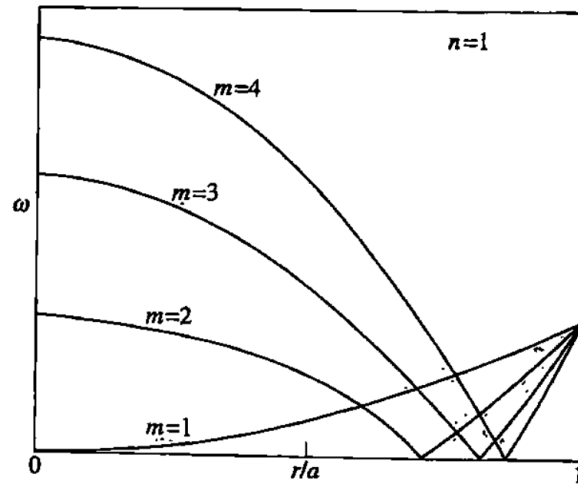Figure A.1: Cylindrical GAE continua for mode numbers $n = 1$ and $m = -1, -2$, and -3.[63]

Figure A.2: Cylindrical GAE continua for mode numbers $n = 1$ and $m = 1, 2, 3$, and 4.[64]
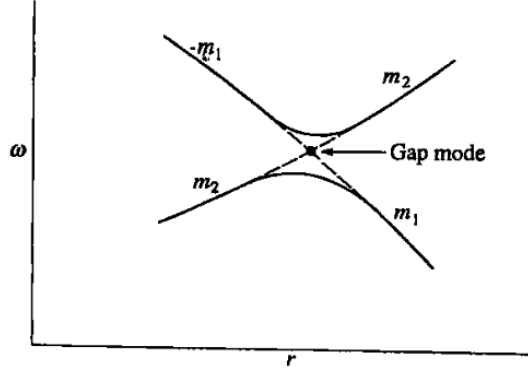
73

Figure A.3: Schematic drawing of TAE gap for mode numbers $n = 1$ and $m = m_1$ and m_2.[64]

Let us consider a toroidal plasma. In this geometry, there is an interaction between the poloidal Fourier components because of toroidal coupling. For a given n, the continuum break and join at their intersections, and gaps appear as shown in Fig. A.3[64]. There is a mode within the gap, and the mode is called toroidal Alfvén eigenmode (TAE) because the gap is created by toroidicity. Now we know there are two important characteristics of TAE. Firstly, the mode is located inside the gap. Secondly, there are two different continua near the gap, that means there are two dominant poloidal modes. As we know, it is caused by toroidicity. Then, the eigenmode is called toroidicity-induced Alfvén eigenmode (TAE).

Numerical analyses revealed another type of gap mode in reversed shear plasmas.[52] This mode is called reversed shear Alfvén eigenmode (RSAE) that peaks near the location of the minimum safety factor value (q_{min}). R-SAE consists of one dominant poloidal mode number. It is irrelevant to the toroidicity-induced gap. The frequency of RSAE is sensitive to q_{min} value.
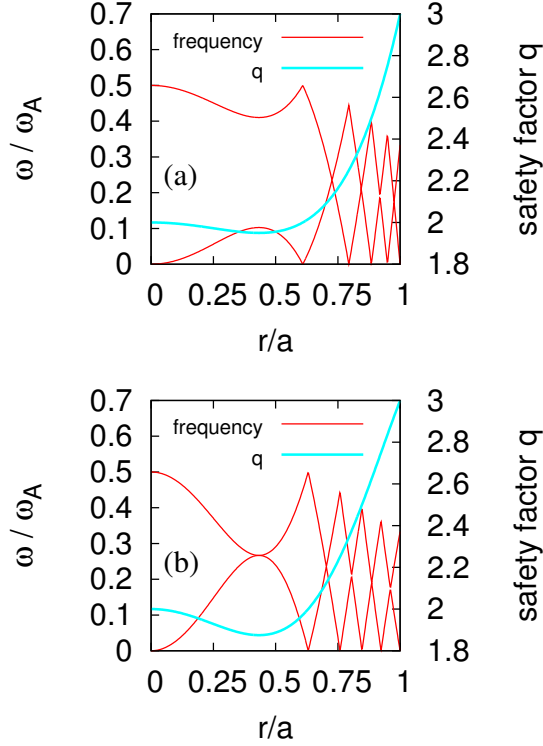
Figure A.4: Alfvén continua for (a) RSAE and (b) TAE in cylindrical plasmas without toroidicity.

A.2 Comparison of continua without toroidicity

In the present thesis, toroidicity is considered in Fig. 3.1 in chapter 3. However, it is not clear whether the toroidicity has the same influence on the continuum gaps in the two panels. Figure A.4 shows the Alfvén continua of the cylindrical plasma without toroidicity. We see in Fig. A.4(b) the gap is closed for the TAE mode. Then, we can understand that the gap in Fig. 3.1(b) is created by toroidicity. For the RSAE case, the gap still exists in the cylindrical plasma. The gap is created by reversed shear and independent of toroidicity.

75

Appendix B

Energetic Particle Orbit Width

In the Fig. 3.5, we see the energetic particle transport takes place in the whole plasma while the modes are located around $r/a = 0.4$. The key point to understand the ubiquitous transport is the orbit width. When a particle moves in the toroidal plasma, the orbit deviates from the magnetic surface and the deviation is called the orbit width.[65, 66] Neglecting the velocity variation due to the mirror force, the orbit width is given by

$$|W| = \left| \frac{mv_\parallel}{QB} q(1 + \frac{v_\perp^2}{2v_\parallel^2}) \right|, \tag{B.1}$$

where Q is the particle charge and q is the safety factor. Consider $v^2 = v_\parallel^2 + v_\perp^2$, the above equation can be rewritten as

$$|W| = \left| \frac{mv_\parallel}{QB} q(1 + \frac{v^2 - v_\parallel^2}{2v_\parallel^2}) \right|. \tag{B.2}$$

In the present Alfvén eigenmode simulation, the absolute value of orbit width $|W|$ depends on $v_\parallel$, q and $v_\parallel/v$. When the absolute value of orbit width is large enough, particles can move from plasma center to edge, sometimes farther.

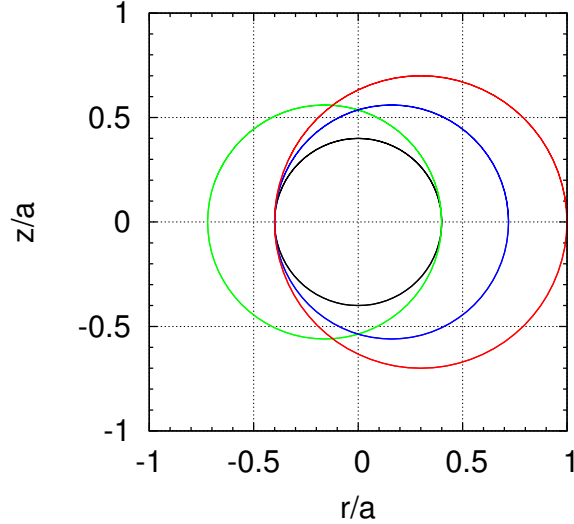In order to calculate $|W|$, we assume that $q = 1.9$ in Fig. 3.5. Under

Figure B.1: Particle orbits and a magnetic surface. Blue and green curves represent the orbits of co- and counter-going particles with $v_\parallel = v$. Red circle represents the orbit of co-going particle with $v_\parallel = 0.3v$. Black circle represents a magnetic surface.

the extreme condition of $v_\parallel/v = 1$ and $v_\perp = 0$, then $|W| = 0.32a$ and this is the minimum value. As the mode peaks around $r/a = 0.4$, the particle transport can take place even at $r/a = 0.4 + 0.32 = 0.72$ as shown in Fig. B.1. The particles co-going to the plasma current shift to the low field side while counter-going particles shift to the high field side. Both of the left edge of green circle and the right edge of the blue circle reach $r/a = 0.72$.

The absolute value of orbit width increases as $v_\parallel/v$ decreases. If $v_\parallel/v = 0.295$, then $|W|$ can increase to $0.6a$, and the particles can move to the plasma boundary as shown in Fig. B.1. The red circle touches the boundary. Since the pitch angle distribution is uniform for Alfvén eigenmode simulation, many particles' orbit width can exceed $0.6a$. Furthermore, we should consider the finite width of the Alfvén eigenmode spatial profiles. Indeed, the modes have

substantial amplitude outside $r/a = 0.4$ as shown in Fig. 3.2. In addition, q value increases at larger radius leading to the larger obit width. For $v_\parallel/v = 0.295$ case, the orbit circle is larger than the red one in Fig. B.1. Then, the particle transport can take place near the plasma edge, even if the particles interact with the eigenmode near the mode peak location $r/a \sim 0.4$.

Bibliography

[1] J. Wesson. *Tokamaks*. International Series of Monographs on Physics. Oxford University Press, 2011.

[2] F. Bortz. *Meltdown!: The Nuclear Disaster in Japan and Our Energy Future*. Single Titles. Twenty First Century Books, 2012.

[3] F.F. Chen. *Introduction to Plasma Physics and Controlled Fusion: Plasma physics*. Introduction to Plasma Physics and Controlled Fusion. Plenum Press, 1984.

[4] M. Kikuchi. *Frontiers in Fusion Research: Physics and Fusion*. Springer, 2011.

[5] W. W. Heidbrink, N. N. Gorelenkov, Y. Luo, M. A. Van Zeeland, R. B. White, M. E. Austin, K. H. Burrell, G. J. Kramer, M. A. Makowski, G. R. McKee, and R. Nazikian. Anomalous flattening of the fast-ion profile during alfvén-eigenmode activity. *Phys. Rev. Lett.*, 99:245002, Dec 2007.

[6] Niels Winsor, John L. Johnson, and John M. Dawson. Geodesic acoustic waves in hydromagnetic systems. *Physics of Fluids*, 11:2448–2450, 1968.

[7] H. Sugama and T.-H. Watanabe. Dynamics of zonal flows in helical systems. *Phys. Rev. Lett.*, 94:115001, Mar 2005.

[8] H. Sugama and T.-H. Watanabe. Collisionless damping of zonal flows in helical systems. *Physics of Plasmas*, 13(1):012501–012501–18, 2006.

[9] P H Diamond, S-I Itoh, K Itoh, and T S Hahm. Zonal flows in plasma—a review. *Plasma Physics and Controlled Fusion*, 47(5):R35, 2005.

[10] Y. Todo, H.L. Berk, and B.N. Breizman. Nonlinear magnetohydrodynamic effects on alfvén eigenmode evolution and zonal flow generation. *Nuclear Fusion*, 50(8):084016, 2010.

[11] H.L. Berk, C.J. Boswell, D. Borba, A.C.A. Figueiredo, T. Johnson, M.F.F. Nave, S.D. Pinches, S.E. Sharapov, and JET EFDA contributors. Explanation of the jet n = 0 chirping mode. *Nuclear Fusion*, 46(10):S888, 2006.

[12] R. Nazikian, G. Y. Fu, M. E. Austin, H. L. Berk, R. V. Budny, N. N. Gorelenkov, W. W. Heidbrink, C. T. Holcomb, G. J. Kramer, G. R. McKee, M. A. Makowski, W. M. Solomon, M. Shafer, E. J. Strait, and M. A. Van Zeeland. Intense geodesic acousticlike modes driven by suprathermal ions in a tokamak plasma. *Phys. Rev. Lett.*, 101:185001, Oct 2008.

[13] G. Y. Fu. Energetic-particle-induced geodesic acoustic mode. *Phys. Rev. Lett.*, 101:185002, Oct 2008.

[14] H.L. Berk and T. Zhou. Fast excitation of egam by nbi. *Nuclear Fusion*, 50(3):035007, 2010.

[15] T. Ido, A. Shimizu, M. Nishiura, S. Nakamura, S. Kato, H. Nakano, Y. Yoshimura, K. Toi, K. Ida, M. Yoshinuma, S. Satake, F. Watanabe, S. Morita, M. Goto, K. Itoh, S. Kubo, T. Shimozuma, H. Igami, H. Takahashi, I. Yamada, K. Narihara, and the LHD Experiment Group. Potential fluctuation associated with the energetic-particle-induced geodesic

acoustic mode in the large helical device. *Nuclear Fusion*, 51(7):073046, 2011.

[16] K. Toi, F. Watanabe, T. Tokuzawa, K. Ida, S. Morita, T. Ido, A. Shimizu, M. Isobe, K. Ogawa, D. A. Spong, Y. Todo, T. Watari, S. Ohdachi, S. Sakakibara, S. Yamamoto, S. Inagaki, K. Narihara, M. Osakabe, K. Nagaoka, Y. Narushima, K. Y. Watanabe, H. Funaba, M. Goto, K. Ikeda, T. Ito, O. Kaneko, S. Kubo, S. Murakami, T. Minami, J. Miyazawa, Y. Nagayama, M. Nishiura, Y. Oka, R. Sakamoto, T. Shimozuma, Y. Takeiri, K. Tanaka, K. Tsumori, I. Yamada, M. Yoshinuma, K. Kawahata, and A. Komori. Observation of reversed-shear alfvén eigenmodes excited by energetic ions in a helical plasma. *Phys. Rev. Lett.*, 105:145003, Oct 2010.

[17] Y. Todo and T. Sato. Linear and nonlinear particle-magnetohydrodynamic simulations of the toroidal alfvén eigenmode. *Physics of Plasmas*, 5(5):1321–1327, 1998.

[18] Y Todo. Properties of energetic-particle continuum modes destabilized by energetic ions with beam-like velocity distributions. *Physics of Plasmas*, 13:082503, 2006.

[19] C.K. Birdsall and A.B. Langdon. *Plasma physics via computer simulation*. Adam Hilger series on plasma physics. Adam Hilger, 1991.

[20] W. Park, S. Parker, H. Biglari, M. Chance, L. Chen, C. Z. Cheng, T. S. Hahm, W. W. Lee, R. Kulsrud, D. Monticello, L. Sugiyama, and R. White. Threedimensional hybrid gyrokineticmagnetohydrodynamics simulation. *Physics of Plasmas*, 4(7):2033–2037, 1992.

[21] D. A. Spong, B. A. Carreras, and C. L. Hedrick. Linearized gyrofluid model of the alphadestabilized toroidal alfvén eigenmode with continuum damping effects. *Physics of Plasmas*, 4(10):3316–3328, 1992.

[22] Y. Todo, T. Sato, K. Watanabe, T. H. Watanabe, and R. Horiuchi. Magnetohydrodynamic vlasov simulation of the toroidal alfvén eigenmode. *Physics of Plasmas*, 2(7):2711–2716, 1995.

[23] S. Briguglio, G. Vlad, F. Zonca, and C. Kar. Hybrid magnetohydrodynamicgyrokinetic simulation of toroidal alfvén modes. *Physics of Plasmas*, 2(10):3711–3723, 1995.

[24] John M. Dawson. Particle simulation of plasmas. *Rev. Mod. Phys.*, 55:403–447, Apr 1983.

[25] S Usami. Particle simulation and extension to multi-hierarchy model. In *Sokendai Asian Winter School 2011*, Toki, Japan, Feb. 2012.

[26] A.M. Dimits and W.W. Lee. Partially linearized algorithms in gyrokinetic particle simulation. *Journal of Computational Physics*, 107(2):309 – 323, 1993.

[27] S. E. Parker and W. W. Lee. A fully nonlinear characteristic method for gyrokinetic simulation. *Physics of Plasmas*, 5(1):77–86, 1993.

[28] A. Y. Aydemir. A unified monte carlo interpretation of particle simulations and applications to nonneutral plasmas. *Physics of Plasmas*, 1(4):822–831, 1994.

[29] Ritoku Horiuchi and Tetsuya Sato. Full magnetohydrodynamic simulation of the tilting instability in a fieldreversed configuration. *Physics of Plasmas*, 1(3):581–590, 1989.

[30] Y Todo. Introduction to mhd simulation. In *Sokendai Asian Winter School 2011*, Toki, Japan, Feb. 2012.

[31] Naoki Mizuguchi. *Simulation Study of Relaxation Phenomena in Spherical Tokamak*. PhD thesis, The Graduate University for Advanced Studies, 1999.

[32] E. Süli and D.F. Mayers. *An Introduction to Numerical Analysis*. Cambridge University Press, 2003.

[33] R. G. Littlejohn. Variational principles of guiding centre motion. *Journal of Plasma Physics*, 29(01):111–125, 1983.

[34] Y. Kusama, H. Kimura, T. Ozeki, M. Saigusa, G.J. Kramer, T. Oikawa, S. Moriyama, M. Nemoto, T. Fujita, K. Tobita, G.Y. Fu, R. Nazikian, and C.Z. Cheng. Toroidal alfvén eigenmodes driven with icrf accelerated protons in jt-60u negative shear discharges. *Nuclear Fusion*, 38(8):1215, 1998.

[35] H. Kimura, Y. Kusama, M. Saigusa, G.J. Kramer, K. Tobita, M. Nemoto, T. Kondoh, T. Nishitani, O. Da Costa, T. Ozeki, T. Oikawa, S. Moriyama, A. Morioka, G.Y. Fu, C.Z. Cheng, and V.I. Afanas'ev. Alfvén eigenmode and energetic particle research in jt-60u. *Nuclear Fusion*, 38(9):1303, 1998.

[36] M. Takechi, A. Fukuyama, M. Ishikawa, C. Z. Cheng, K. Shinohara, T. Ozeki, Y. Kusama, S. Takeji, T. Fujita, T. Oikawa, T. Suzuki, N. Oyama, A. Morioka, N. N. Gorelenkov, G. J. Kramer, and R. Nazikian. Alfvén eigenmodes in reversed shear plasmas in jt-60u negative-ion-based neutral beam injection discharges. *Physics of Plasmas*, 12(8):082509–082509–7, 2005.

[37] J A Snipes, A Fasoli, P Bonoli, S Migliuolo, M Porkolab, J E Rice, Y Takase, and S M Wolfe. Investigation of fast particle driven modes on alcator c-mod. *Plasma Physics and Controlled Fusion*, 42(4):381, 2000.

[38] S.E Sharapov, D Testa, B Alper, D.N Borba, A Fasoli, N.C Hawkes, R.F Heeter, M Mantsinen, and M.G Von Hellermann. Mhd spectroscopy through detecting toroidal alfvén eigenmodes and alfvén wave cascades. *Physics Letters A*, 289(3):127 – 134, 2001.

[39] R. Nazikian, G. J. Kramer, C. Z. Cheng, N. N. Gorelenkov, H. L. Berk, and S. E. Sharapov. New interpretation of alpha-particle-driven instabilities in deuterium-tritium experiments on the tokamak fusion test reactor. *Phys. Rev. Lett.*, 91:125003, Sep 2003.

[40] M A Van Zeeland, G J Kramer, R Nazikian, H L Berk, T N Carlstrom, and W M Solomon. Alfvén eigenmode observations on diii-d via two-colour co 2 interferometry. *Plasma Physics and Controlled Fusion*, 47(9):L31, 2005.

[41] M. Takechi, G. Matsunaga, K. Toi, M. Isobe, T Minami, K. Tanaka, S. Nishimura, C. Takahashi, S. Okamura, and K. Matsuoka. Transition of toroidal alfvén eigenmode to global alfvén eigenmode in chs heliotron/torsatron plasmas heated transition of toroidal alfvén eigenmode to global alfvén eigenmode in chs heliotron/torsatron plasmas heated by neutral beam injection. *J. Plasma Fusion Res.*, 78:1273, 2002.

[42] K Toi, S Yamamoto, N Nakajima, S Ohdachi, S Sakakibara, M Osakabe, S Murakami, K Y Watanabe, M Goto, K Kawahata, Ya I Kolesnichenko, S Masuzaki, S Morita, K Narihara, Y Narushima, Y Takeiri, K Tanaka, T Tokuzawa, H Yamada, I Yamada, K Yamazaki, and LHD Experimental Group. Energetic ion driven alfvén eigenmodes in large helical

device plasmas with three-dimensional magnetic structure and their impact on energetic ion transport. *Plasma Physics and Controlled Fusion*, 46(7):S1, 2004.

[43] A. Fukuyama and T. Tohnai. Kinetic analysis of tae in tokamaks and helical devices. In *Proc.of 5th TCM on Alpha Particles in Fusion Research.*, Abingdon, UK, 8-11 September 1997.

[44] A. Fukuyama and E. Yokota. *Proceedings of the 6th IAEA Technical Committee Meeting on Energetic Particles in Magnetic Confinement Systems: October 12-14, 1999, JAERI, Naka, Japan.* JAERI-Conf. Japan Atomic Energy Research Institute, 2000.

[45] C.Z Cheng, Liu Chen, and M.S Chance. High-n ideal and resistive shear alfvén waves in tokamaks. *Annals of Physics*, 161(1):21 – 47, 1985.

[46] C. Z. Cheng and M. S. Chance. Lown shear alfvén spectra in axisymmetric toroidal plasmas. *Physics of Fluids*, 29(11):3695–3701, 1986.

[47] B. N. Breizman, H. L. Berk, M. S. Pekker, S. D. Pinches, and S. E. Sharapov. Theory of alfvén eigenmodes in shear reversed plasmas. *Physics of Plasmas*, 10(9):3649–3660, 2003.

[48] H. L. Berk, D. N. Borba, B. N. Breizman, S. D. Pinches, and S. E. Sharapov. Theoretical interpretation of alfvén cascades in tokamaks with nonmonotonic q profiles. *Phys. Rev. Lett.*, 87:185002, Oct 2001.

[49] F. Zonca, S. Briguglio, L. Chen, S. Dettrick, G. Fogaccia, D. Testa, and G. Vlad. Energetic particle mode stability in tokamaks with hollow q-profiles. *Physics of Plasmas*, 9(12):4939–4956, 2002.

[50] G J Kramer, N N Gorelenkov, R Nazikian, and C Z Cheng. Finite pressure effects on reversed shear alfvén eigenmodes. *Plasma Physics and Controlled Fusion*, 46(11):L23, 2004.

[51] B. N. Breizman, M. S. Pekker, S. E. Sharapov, and JET EFDA contributors. Plasma pressure effect on alfvén cascade eigenmodes. *Physics of Plasmas*, 12(11):112506–112506–9, 2005.

[52] A. Fukuyama and T. Akutsu. Kinetic global analysis of alfven eigenmodes in toroidal plasmas. In *Proc. 19th Int. Conf. Fusion Energy (Lyon, 2002), CD-ROM TH/P3-14*, Lyon, 2002.

[53] Y. Todo, K. Shinohara, M. Takechi, and M. Ishikawa. Nonlocal energetic particle mode in a jt-60u plasma. *Physics of Plasmas*, 12(1):012503–012503–7, 2005.

[54] G. Y. Fu and J. W. Van Dam. Excitation of the toroidicityinduced shear alfvén eigenmode by fusion alpha particles in an ignited tokamak. *Physics of Plasmas*, 1(10):1949–1952, 1989.

[55] Fulvio Zonca and Liu Chen. Resonant damping of toroidicity-induced shear-alfvén eigenmodes in tokamaks. *Phys. Rev. Lett.*, 68:592–595, Feb 1992.

[56] M. N. Rosenbluth, H. L. Berk, J. W. Van Dam, and D. M. Lindberg. Continuum damping of high-mode-number toroidal alfvén waves. *Phys. Rev. Lett.*, 68:596–599, Feb 1992.

[57] Zhiyong Qiu, Fulvio Zonca, and Liu Chen. Nonlocal theory of energetic-particle-induced geodesic acoustic mode. *Plasma Physics and Controlled Fusion*, 52(9):095003, 2010.

[58] G. Y. FU. On nonlinear self-interaction of geodesic acoustic mode driven by energetic particles. *Journal of Plasma Physics*, 77(04):457–467, 2011.

[59] Deng Zhou. Electromagnetic geodesic acoustic modes in tokamak plasmas. *Physics of Plasmas*, 14(10):104502–104502–4, 2007.

[60] H. L. Berk, B. N. Breizman, J. Candy, M. Pekker, and N. V. Petviashvili. Spontaneous hole–clump pair creation. *Physics of Plasmas*, 6:3102–3113, 1999.

[61] W W Heidbrink, E Ruskov, E D Fredrickson, N Gorelenkov, S S Medley, H L Berk, and R W Harvey. Weak effect of ion cyclotron acceleration on rapidly chirping beam-driven instabilities in the national spherical torus experiment. *Plasma Physics and Controlled Fusion*, 48(9):1347, 2006.

[62] Yan Ming Li, Swadesh M. Mahajan, and David W. Ross. Destabilization of global alfvén eigenmodes and kinetic alfvén waves by alpha particles in a tokamak plasma. *Physics of Fluids*, 30(5):1466–1484, 1987.

[63] G. Y. Fu and J. W. Van Dam. Stability of the global alfvén eigenmode in the presence of fusion alpha particles in an ignited tokamak plasma. *Physics of Plasmas*, 1(12):2404–2413, 1989.

[64] J. Wesson and D.J. Campbell. *Tokamaks*. International series of monographs on physics. Clarendon Press, 2004.

[65] K. Miyamoto. *Fundamentals of Plasma Physics and Controlled Fusion*. NIFS-PROC. National Institute for Fusion Science, 2000.

[66] J.P. Freidberg. *Plasma Physics And Fusion Energy*. Cambridge University Press, 2007.